

## 4 Validation Testing and Round-Robin SCC Crack-Growth Rate Testing

### 4.1 Cold-Worked Austenitic Stainless Steels

Cold-worked 316SS compact tension samples were inserted into the autoclaves during shakedown testing and were used as one means to evaluate the capability of the PNNL systems to generate crack-growth data consistent with crack-growth data published in the literature. Cold-worked 316SS was used because there is much data in the literature on this material, and the material readily cracks with a predictable response. The compositions and mechanical condition for the three different heats of 316SS that were tested are shown in Table 4.1.

**Table 4-1 Type 316SS Heats**

Material - Source	Heat No. and Description	Composition, wt%
316SS – Heat #1 PNNL	PNNL1, 20% CW (No records on Heat No.)	Fe-16.8Cr-11.4Ni-2.3Mo-1.9Mn-0.5Si- 0.05C-0.02N-0.013S-0.018P
316SS – Heat #2 PNNL	PNNL2, 20% CW (No records on Heat No.)	Fe-17.6Cr-13.4Ni-2.3Mo-1.8Mn-0.44Si- 0.06C-0.05N-0.013S-0.013P
316LSS – Heat #3 GEG	A14128, 21% CW at 140°C	Fe-17.6Cr-12.4Ni-2.6Mo-1.8Mn-0.5Si- 0.014C-0.085N

The first test was on a 1T CT sample from 316SS heat #1 with no side grooves. This sample was air pre-cracked prior to being inserted into the autoclave. The reason for pre-cracking ex-situ was to get some hands-on experience with running the servohydraulic machine using the GEG software. The pre-cracking curve is shown in Figure 4.1. The pre-cracking steps shown along the top of the plot are more aggressive than what is usually done, but still illustrate the pre-cracking progression. The dcPd data for this exercise were extremely noisy, and the issue that was causing the noise has since been determined and corrected. After air pre-cracking, the sample was loaded into System #1 for SCC testing.

The overall crack growth curve in BWR oxidizing water (288°C/550°F, 2000 ppb O<sub>2</sub>) is shown in Figure 4.2. As part of the process of learning about the operation of the equipment, the goal of this test was to look at the effect of different K values on the propagation rate. Testing was performed at three different K values, and at each successively lower K, the CGR rate dropped as demonstrated in Figure 4.2. Conventional theory states that there is a threshold K value below which SCC will cease, but that K value was not reached in this test. After running through the decreasing K values, the K value was then increased back up to the starting value, and the resulting CGR increased back up to the value ( $1.1 \times 10^{-7}$  mm/s) observed previously. From this series of K changes, we were able to observe corresponding reductions in SCC propagation rates and then reestablish the original CGR at higher K. The ability to obtain reproducible CGR response under identical conditions is a key aspect for determining quantitative SCC behavior.

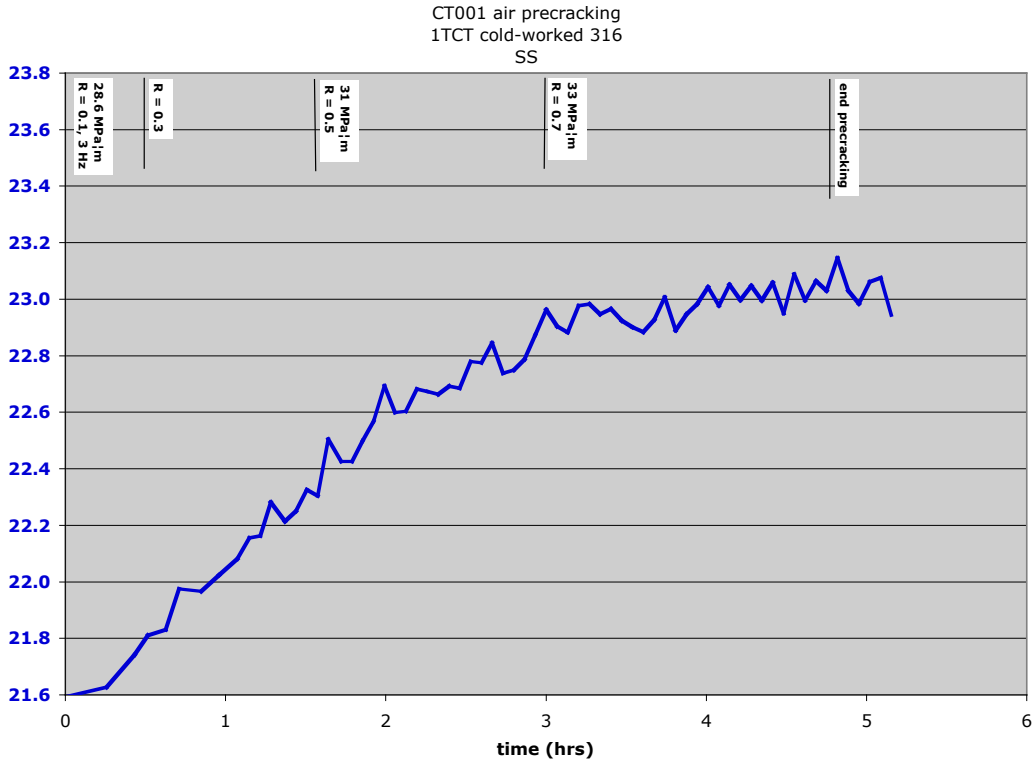


**Figure 4-1 Pre-Cracking Response for CW316SS Sample CT001**

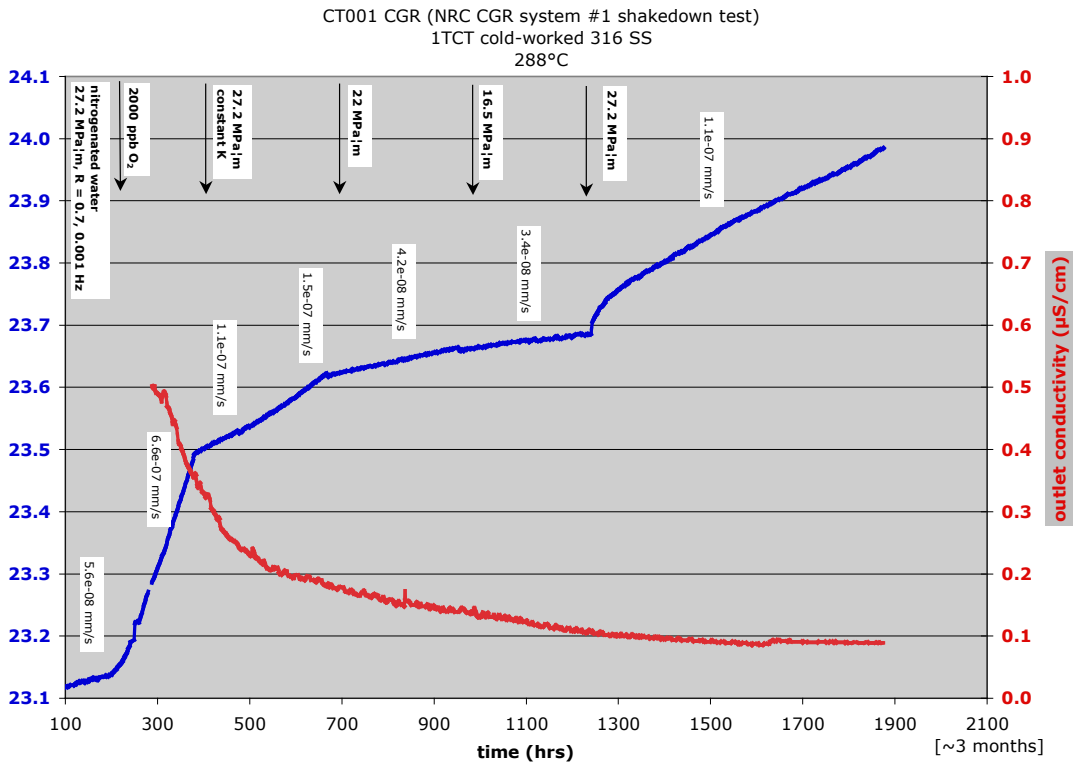


**Figure 4-2 Overall SCC Crack-Growth Response for CW316SS in Test CT001**

The next validation test was to observe the crack growth response of a pair of CW316SS (heat #2) samples in series in System #2. This goal was to demonstrate that we can evaluate samples in series and also to show the ability to apply HWC to reduce the CGR in BWR conditions. For reasons described previously, the two samples were pre-cracked in air prior to being loaded into the autoclave. The pre-cracking curves for CT003 and CT004 are shown in Figures 4.3 and 4.4, respectively. The pre-cracking for CT004 initially started at 20 MPa√m (18.2 ksi√in), but after no increase in crack length was observed after 22 hrs,  $K_{max}$  was increased slightly to 22.5 MPa√m (20.5 ksi√in), which immediately caused a crack to begin growing. Pre-cracking of CT003 was then started at 22.5 MPa√m.

Testing in high-temperature water again began with BWR oxidizing conditions (288°C/550°F, 2000 ppb O<sub>2</sub>). The first phase of the test was to transition from a TG fatigue crack to an intergranular (IG) stress corrosion crack by slowly decreasing the cycle rate and adding a hold time prior to constant K. This response is shown in Figure 4.5. After transitioning to a constant K value of 25 MPa√m (corrected value of 26.5 MPa√m or 24.1 ksi√in), the CGR of both samples settled at  $\sim 4.5 \times 10^{-7}$  mm/s which is typical for a CW316SS in oxidizing water. The next steps in the test were to switch back and forth between normal water chemistry (NWC) and HWC conditions. Under both phases of HWC conditions, the CGR of the samples decreased by  $\sim 100X$  to a rate of approximately  $3 \times 10^{-9}$  mm/s as documented in Figure 4.6.<sup>(a)</sup> When returning to NWC conditions, the CGRs increased back to the original NWC value of  $4.5 \times 10^{-7}$  mm/s. Thus, we were able to produce repeatable behavior on two specimens in series and show that the PNNL test systems produce the expected crack-growth response of 316SS under both BWR oxidizing and HWC conditions.

The third 316SS validation test was performed in System #1. The purpose of this test was re-verify the ability to produce typical crack growth rates in 316SS in BWR NWC and HWC conditions, but this time using a well-characterized stainless steel heat. The material selected was a CW316LSS and has been tested under various CW conditions at GE enabling a direct comparison of SCC crack-growth response.

A rapid transition from the TG fatigue pre-crack to SCC occurred for this test with cycling ended by  $\sim 330$  h and constant K conditions established as shown in Figure 4.7(a). Stable and consistent SCC crack growth ( $\sim 3.5 \times 10^{-7}$  mm/s) was established for the next  $\sim 600$  hours before removing O<sub>2</sub> and adding H<sub>2</sub> at  $\sim 950$  h. This resulted in a rapid decrease in the measured ECPs on the CT sample and on the Pt electrode from  $+0.2 V_{SHE}$  to  $-0.5 V_{SHE}$ . The propagation rate, however, only decreased by  $\sim 40$  percent, which is far less than that documented on the other stainless steel samples. A rate of  $\sim 2 \times 10^{-7}$  mm/s was maintained for  $\sim 500$  h before the decision was made to again re-establish oxidizing water conditions. The CGR after switching back to oxidizing water conditions shows a distinct increase over the next 200 h and reached a value similar to, or slightly greater than seen earlier in the test. During the final testing sequence, stable growth was again established under HWC conditions starting at  $\sim 1850$  h and propagation

---

(a) The increase in outlet conductivity at  $\sim 1300$  h and  $\sim 2200$  h is caused by metal ion release from the autoclave and heated tubing when changing from HWC to NWC. The effect is very large because the autoclave and all the tubing were brand new and had no previous high temperature oxide layer. The increase in outlet conductivity at  $\sim 2700$  h corresponds to the onset of sulfate injection.

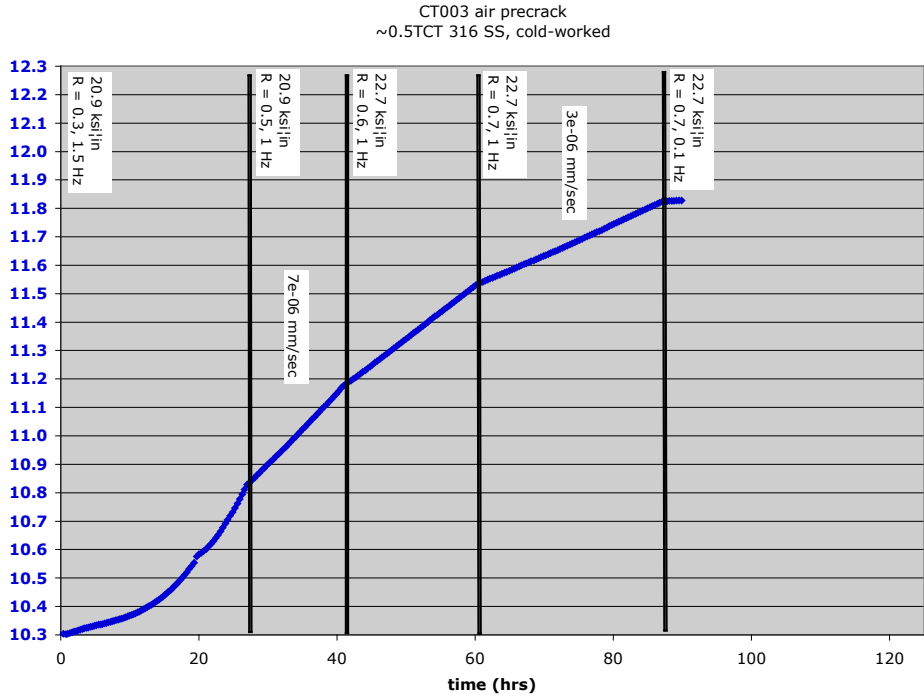


**Figure 4-3 Air Pre-Cracking of Sample CT003**

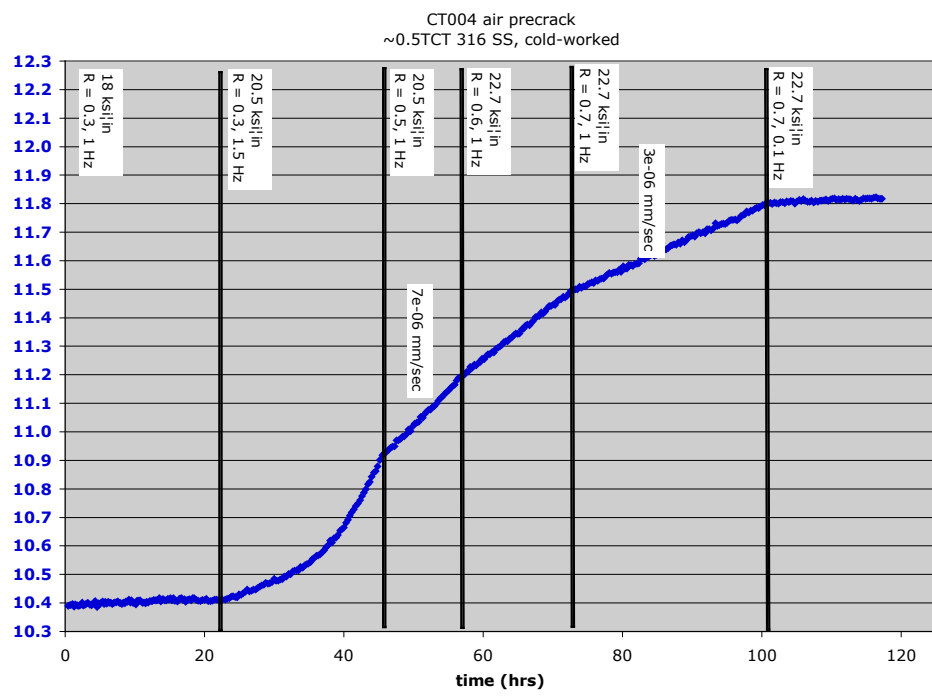


**Figure 4-4 Air Pre-Cracking of Sample CT004**

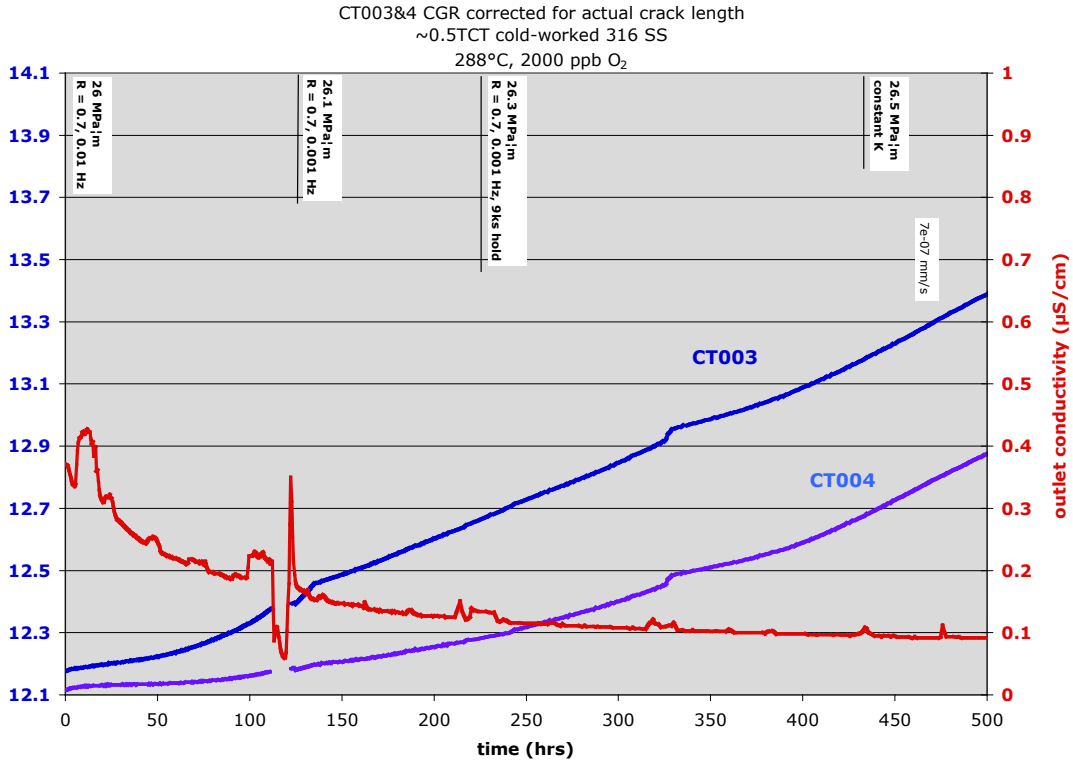


**Figure 4-5 Crack-Transitioning Steps for Samples CT003 and CT004 Tested in Series**

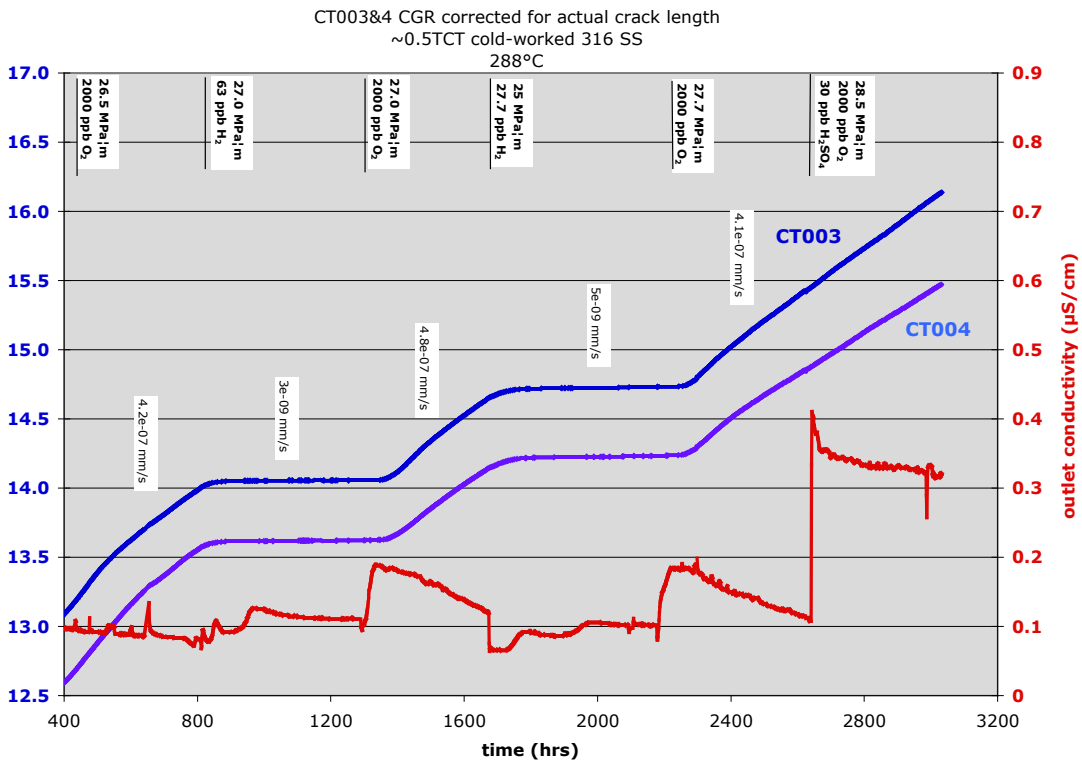
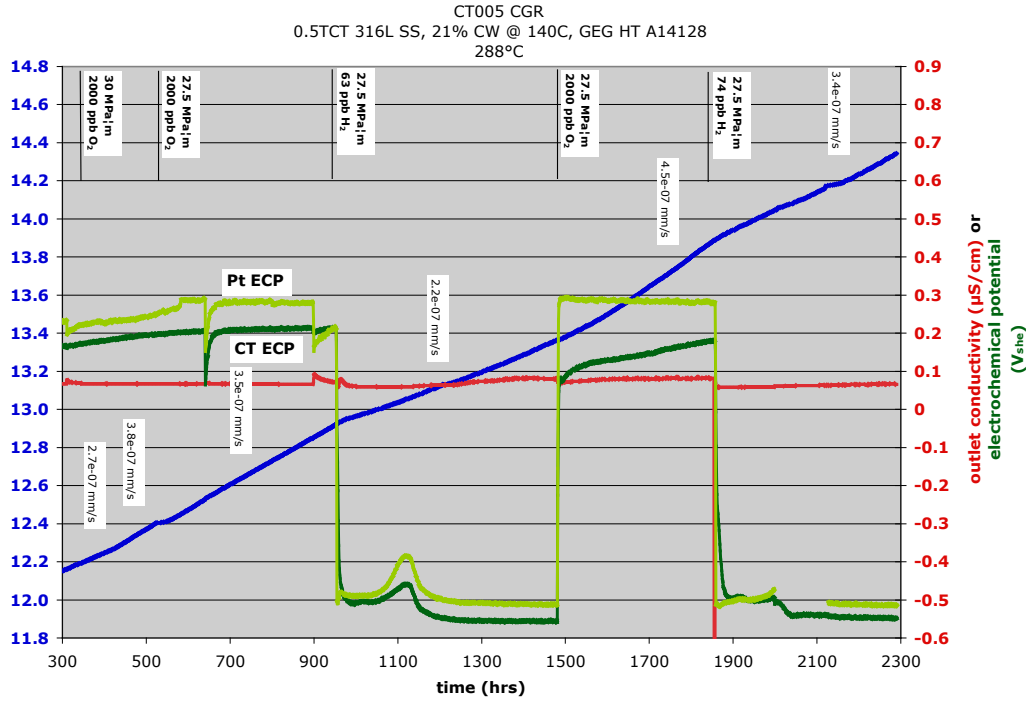
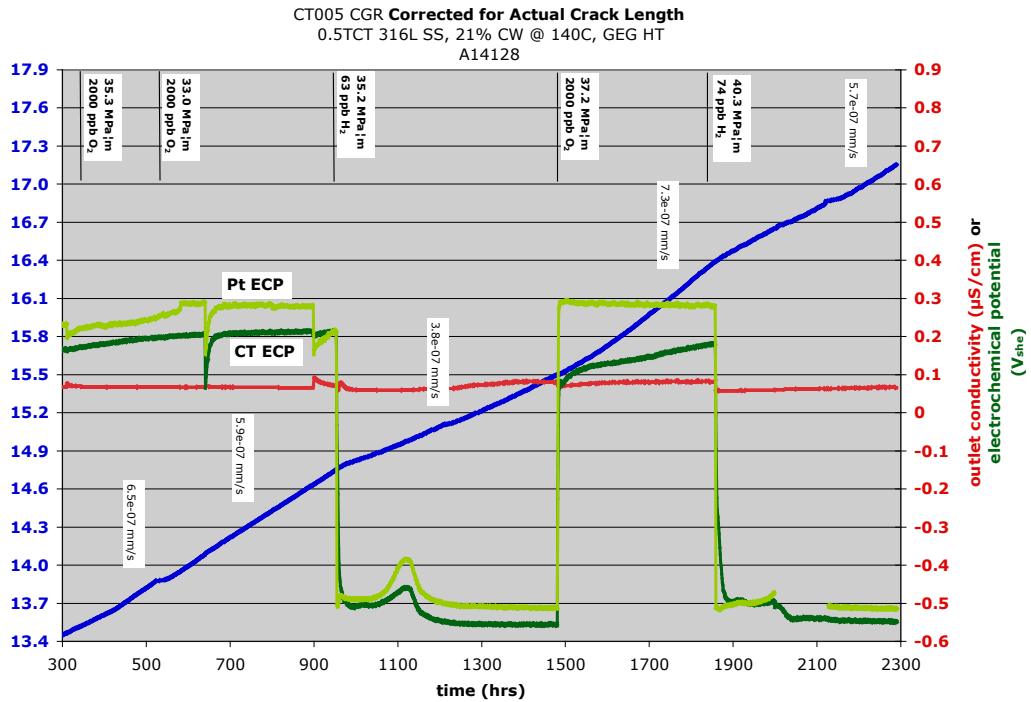


**Figure 4-6 Overview of SCC CGR Response under Constant K Condition Switching from BWR Oxidizing to BWR HWC for CT003 and CT004 Tested in Series**



(a)



(b)

Figure 4-7 Crack-Growth Test for CT005 Sample: (a) full test with uncorrected K levels and crack length, and (b) full test with corrected K levels and crack length

continued at a rate of  $\sim 3 \times 10^{-7}$  mm/s. It was important to repeat these steps and confirm the unexpected SCC behavior at low ECP for this heat of 316LSS. This identical heat has been examined in detail as part of a prior U.S. Department of Energy (DOE) project on SCC crack growth in high-ECP oxidizing BWR water. Comparisons to the SCC tip structures produced under low-ECP, hydrogen-water chemistry will be important to assess mechanistic differences during SCC propagation. Initial examinations are described later in this report in Section 6.4.

A critical result for this sample was discovered during post-test fractography examinations. Measurements of crack extension by dcpd were found to significantly underpredict the actual crack length. Corrected K levels and crack length are shown in Figure 4.7(b). By the end of the test, the K level had increased to approximately 37 percent beyond the validity criterion (Eq. 3.1). This will be discussed in more detail along with the results of a second test on this same heat.

A second test on this heat of material was performed to verify the crack growth and dcpd behavior of this heat of 316LSS. In anticipation of possible large underprediction of crack length again, this second test was set up to initially run at  $25 \text{ MPa}\sqrt{\text{m}}$  ( $22.8 \text{ ksi}\sqrt{\text{in}}$ ) rather than the  $30 \text{ MPa}\sqrt{\text{m}}$  ( $27.3 \text{ ksi}\sqrt{\text{in}}$ ) target in the previous test. Post-test crack length observation revealed that as with the previous test, dcpd significantly underestimated crack length in this second test. The crack growth curve with actual crack length and K values is shown in Figure 4.8. The pre-cracking sequence for this test was identical to the previous test on this material, and after establishing a crack growth rate of  $1.0 \times 10^{-6}$  mm/s at  $27.5$  to  $30 \text{ MPa}\sqrt{\text{m}}$  ( $24.9$  -  $27.3 \text{ ksi}\sqrt{\text{in}}$ ) under NWC conditions,  $\text{O}_2$  was removed and  $1560$  ppb  $\text{H}_2$  was added. As with the prior test (CT005) at a higher K level, rapid crack growth rates under HWC ( $1560$  ppb  $\text{H}_2$ ) of  $3.3 \times 10^{-7}$  mm/s and  $2.3 \times 10^{-7}$  mm/s were measured at  $30 \text{ MPa}\sqrt{\text{m}}$  and  $25 \text{ MPa}\sqrt{\text{m}}$ , respectively, as shown in Figure 4.8. This crack growth rate once again identifies the unique behavior of this 316LSS heat even under valid K values (as defined by Eq. 3.1). The final testing step was to drop the K level to a target value of  $15 \text{ MPa}\sqrt{\text{m}}$  (corrected to  $20 \text{ MPa}\sqrt{\text{m}}$  after post-test examination of actual crack length) and gently cycle the crack ( $0.001$  Hz, then  $0.001$  Hz with  $9000$  s hold). This was done to grow the crack beyond the plastic zone established at the higher K before changing to constant K conditions at  $\sim 2525$  hours. The final 450 hours of the test are shown in Figure 4.9. After transitioning to constant K, a lower CGR is immediately observed and then followed by an increase to a rate of  $\sim 2.5 \times 10^{-8}$  mm/s, which is approximately an order of magnitude lower than the values measured at higher K levels (corrected for actual crack length) earlier in the test as illustrated in Figure 4.8.

It is important to note that dcpd again significantly underpredicted the crack length. In-situ dcpd measurements gave a value for the total crack length of  $\sim 14.42$  mm, while post-test exams revealed the actual crack length to be  $\sim 16.28$  mm. As a result, the target constant K values of  $25$ ,  $20$ , and  $15 \text{ MPa}\sqrt{\text{m}}$  turned out to be  $\sim 30$ ,  $25$ , and  $20 \text{ MPa}\sqrt{\text{m}}$  ( $27.3$ ,  $22.6$ ,  $18.2 \text{ ksi}\sqrt{\text{in}}$ ) after correction. In the end, these corrected values are still within the K validity criterion of  $\sim 32 \text{ MPa}\sqrt{\text{m}}$  ( $29.1 \text{ ksi}\sqrt{\text{in}}$ ).

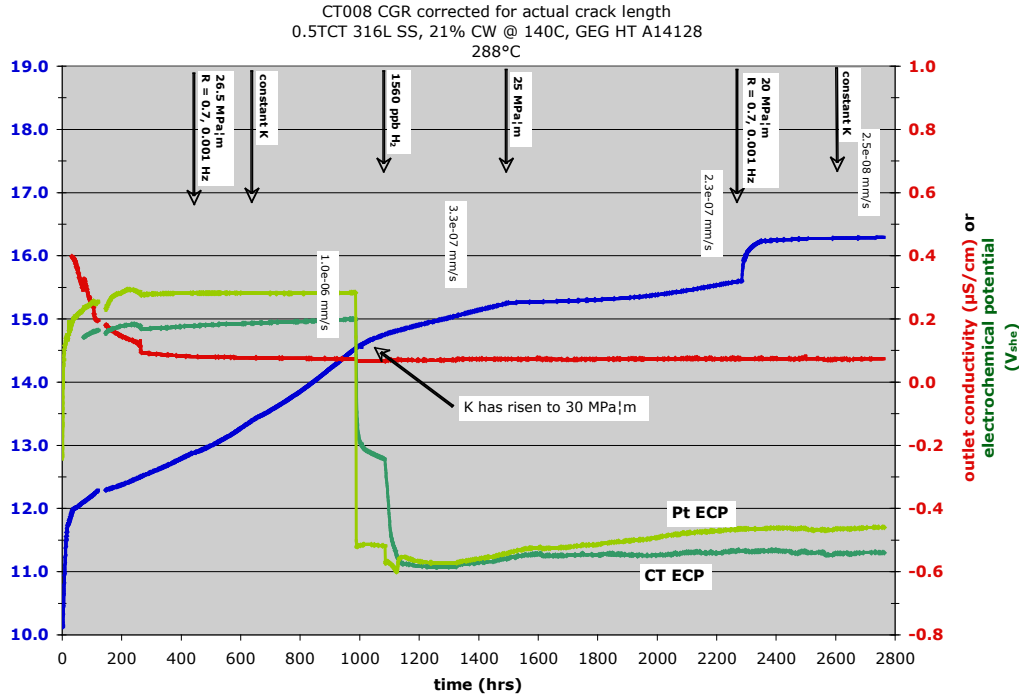


**Figure 4-8 Crack Length, Electrochemical Potential, and Outlet Conductivity Plotted Versus Test Time for the CW316LSS Sample. Corrected K values are shown after post-test examination of the fracture surface.**

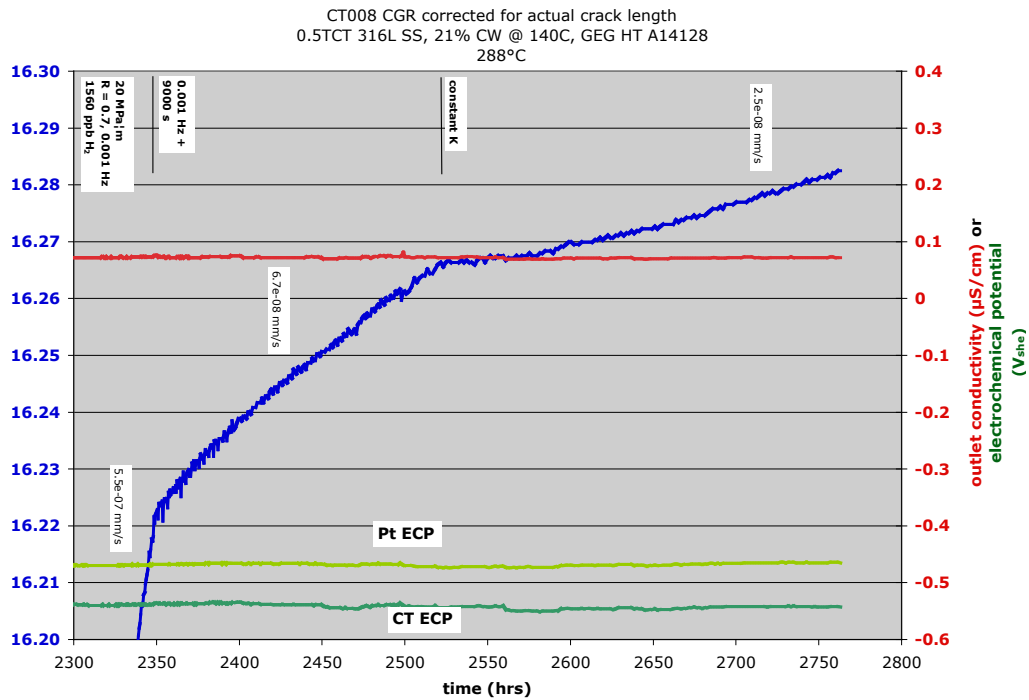


**Figure 4-9 Crack Length, Electrochemical Potential, and Outlet Conductivity Plotted Versus Test Time for the CW316LSS Sample. The final transition to constant K is at 2525 h.**

Metallography and scanning electron microscopy (SEM) were conducted on the crack profile prior to fracturing the sample for crack surface examinations. The sample was cut into two thinner samples, and the crack profile was taken from a surface that represents an interior surface of the original sample. Examples from these examinations are presented in Figures 4.10 and 4.11. Cross-section metallography in Figure 4.10 shows the entire length of the ~6.4-mm-long crack including the initial pre-cracking, crack transitioning, SCC in oxidizing BWR water, and SCC in BWR-HWC conditions documented in Figure 4.8. Cracks are highly branched with what appear to be parallel cracks in some regions. In this cross-section, there are unbroken ligaments as far as 0.65 mm behind the crack tip that suggest unbroken ligaments are playing a role in the crack length underprediction by dcpd. Both IG and TG cracks can be identified in the crack profile throughout the constant K testing under 2000 ppb O<sub>2</sub> and 1560 ppb H<sub>2</sub> conditions. This mixed-mode SCC is better revealed by SEM characterization of the fracture surface as shown in Figure 4.11. The crack front is clearly TG during fatigue pre-cracking and changes to mixed IG and TG during transitioning and the constant K regions. Surprisingly, the distribution of IG and TG is similar during cracking in BWR oxidizing and HWC conditions. Prior work on other CW stainless steels has produced primarily intergranular stress corrosion cracking (IGSCC) during testing in BWR oxidizing water.

The PNNL crack-growth-rate data for CW316SS-type heats are summarized in Figure 4.12 as a function of the corrected crack length and K value. Although we only have a few examples of response under HWC conditions for other 316SS type heats besides the GEG heat A14128, the low propagation rates of these other heats ( $<1 \times 10^{-8}$  mm/s) are consistent with most data in the literature. Current results for the GEG heat show very little improvement over the 2000 ppb O<sub>2</sub> condition and are 50–100X greater than expected under high hydrogen, low ECP conditions.

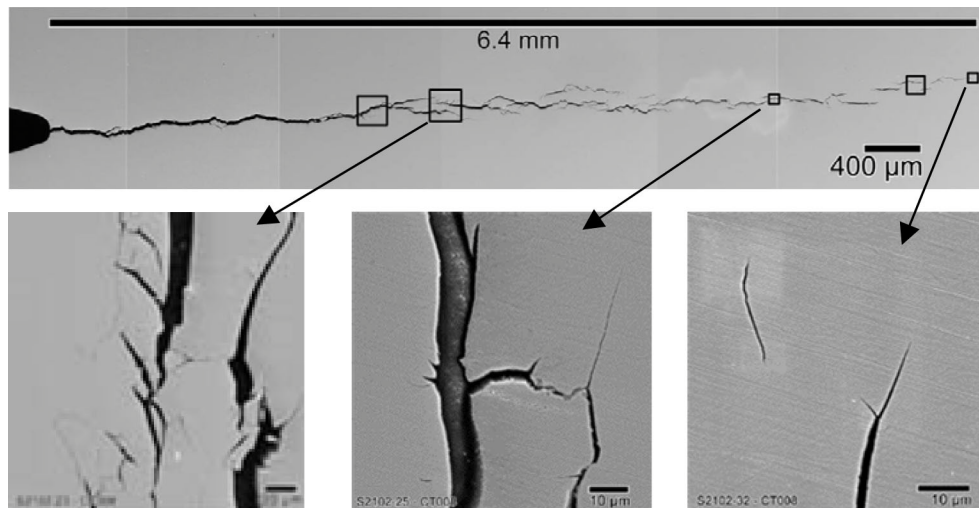


**Figure 4-10 Optical Micrographs Showing Cracks From the Inside Surface of the CW 316LSS CT008 Test Sample. Lower enlarged micrographs need to be rotated by 90° clockwise from image above. Area shown on left is from part of the test in 2000 ppb O<sub>2</sub>, while the areas in the center and on right are during HWC with 1560 ppb H<sub>2</sub>.**

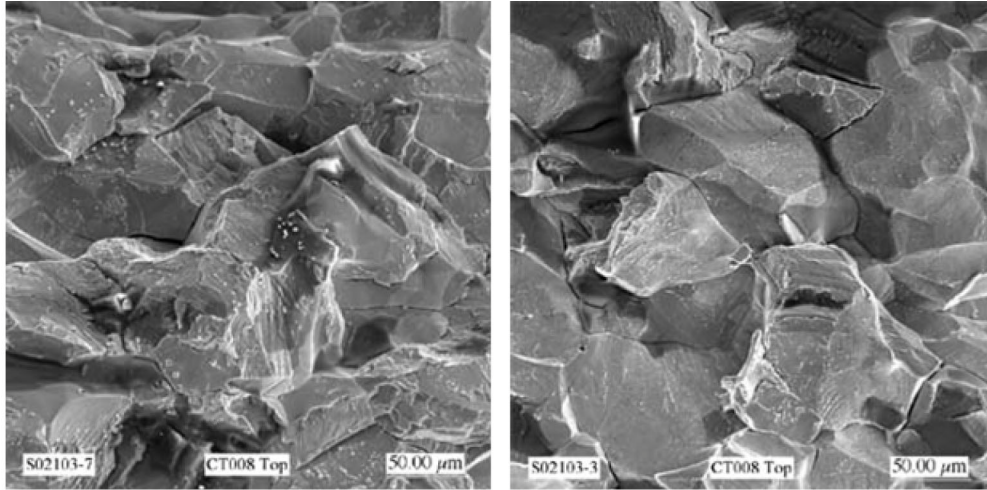


**Figure 4-11 Scanning Electron Micrographs Showing Mixed-Mode, IG/TG Fracture Surface Morphology for CW316LSS CT008 Sample. Area shown on left is from part of the test in 2000 ppb O<sub>2</sub>, while the area on right is during HWC with 1560 ppb H<sub>2</sub>.**

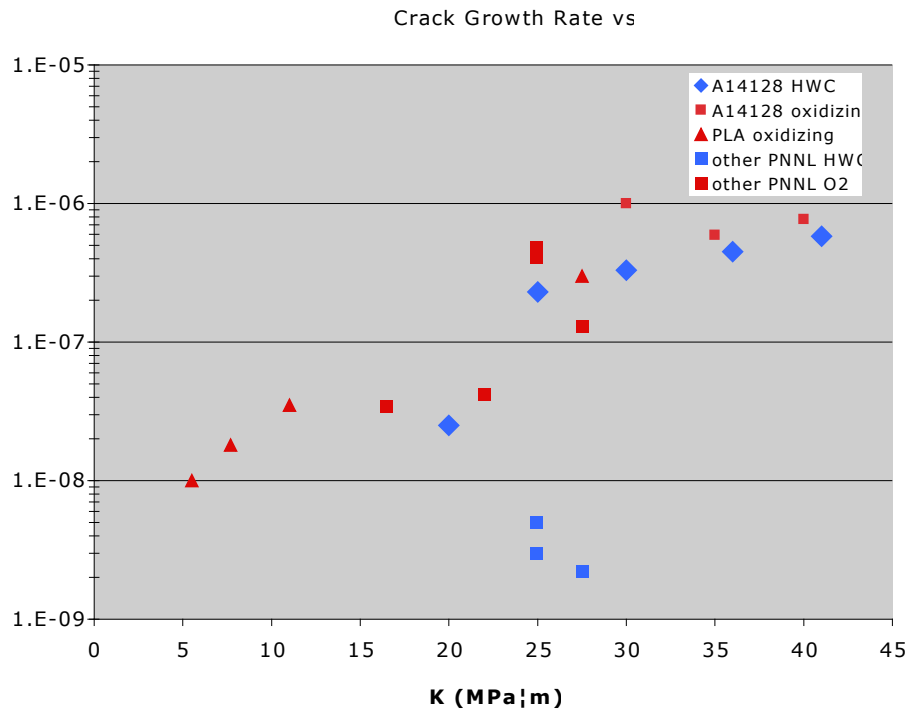


**Figure 4-12 Summary of PNNL Measured Crack-Growth-Rate Data for CW316SS Heats Showing High Propagation Rates for the One Heat under HWC Conditions.**

## 4.2 Alloy 600 and Alloy 182: ICG-EAC Round Robin

Crack-growth-rate testing was performed on a 30-percent CW Alloy 600 0.5T CT sample as part of the International Cooperative Group on Environment-Assisted Cracking (ICG-EAC) round robin. Initial SCC transitioning and early crack-growth response according to a prescribed regiment is summarized in Figure 4.13. Consistent, but slow, crack growth was measured during transitioning to lower cyclic frequencies in steps 6 and 7. Measured growth rates were ~5X lower than anticipated and the step 5 cyclic conditions were re-established at ~1110 h into the test as shown in Figure 4.14. Once again, the crack-growth response at R=0.7 and 0.1 Hz (step 5 conditions) was reasonable, but decreased to low rates when the frequency was dropped to 0.01 Hz when repeating the step #6 conditions. This suggests a difficulty in transitioning from TG corrosion fatigue to IGSCC, and prompted the need for additional intermediate steps. The first attempt was a change in R ratio at ~1275 h from 0.7 to 0.5 while maintaining the reduced cyclic frequency of 0.01 Hz. The initial response was quite promising with the crack-growth rate increasing from ~1 to ~6×10<sup>-7</sup> mm/s, but subsequent steps again demonstrated slow crack-growth under step 6 and 7 conditions. As shown in Figure 4.14, growth rates dropped to ~2×10<sup>-7</sup> mm/s for R=0.7 and 0.01 Hz and to ~4×10<sup>-8</sup> mm/s at 0.001 Hz.

Results from this test have raised concerns for the alloy 600 material and the possibility that stringers of inclusions may be present and promoting off-axis crack extension. Several laboratories participating in the round robin experienced this problem. However based on information from GEG, the section of alloy 600 plate used for our samples did not exhibit such

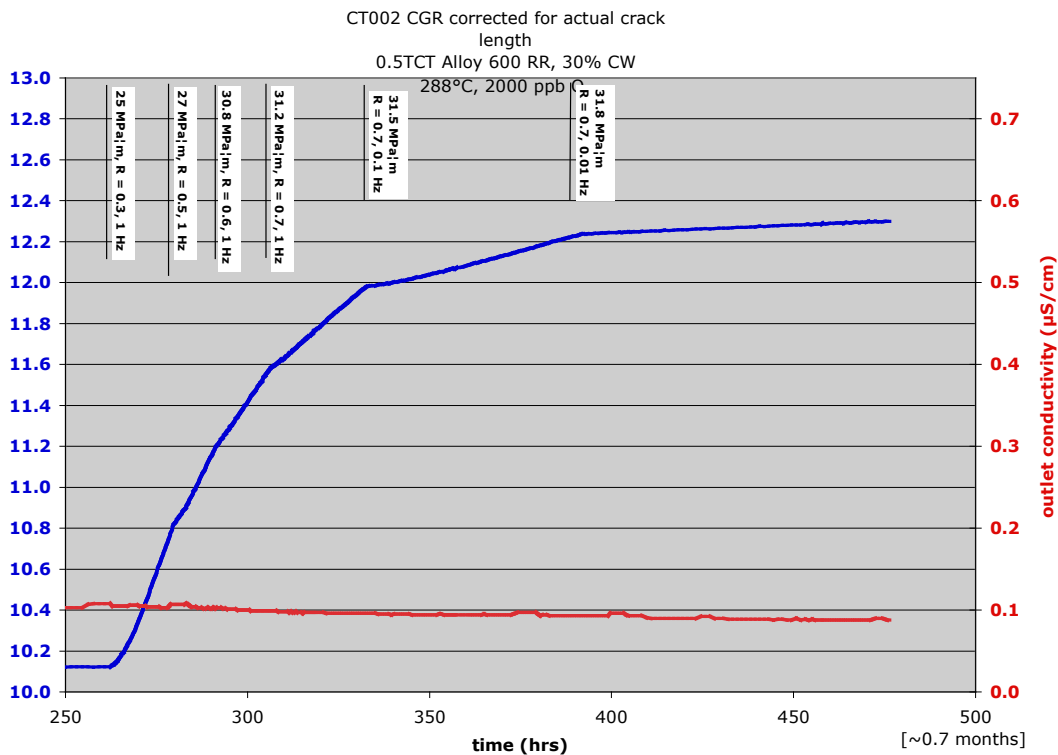
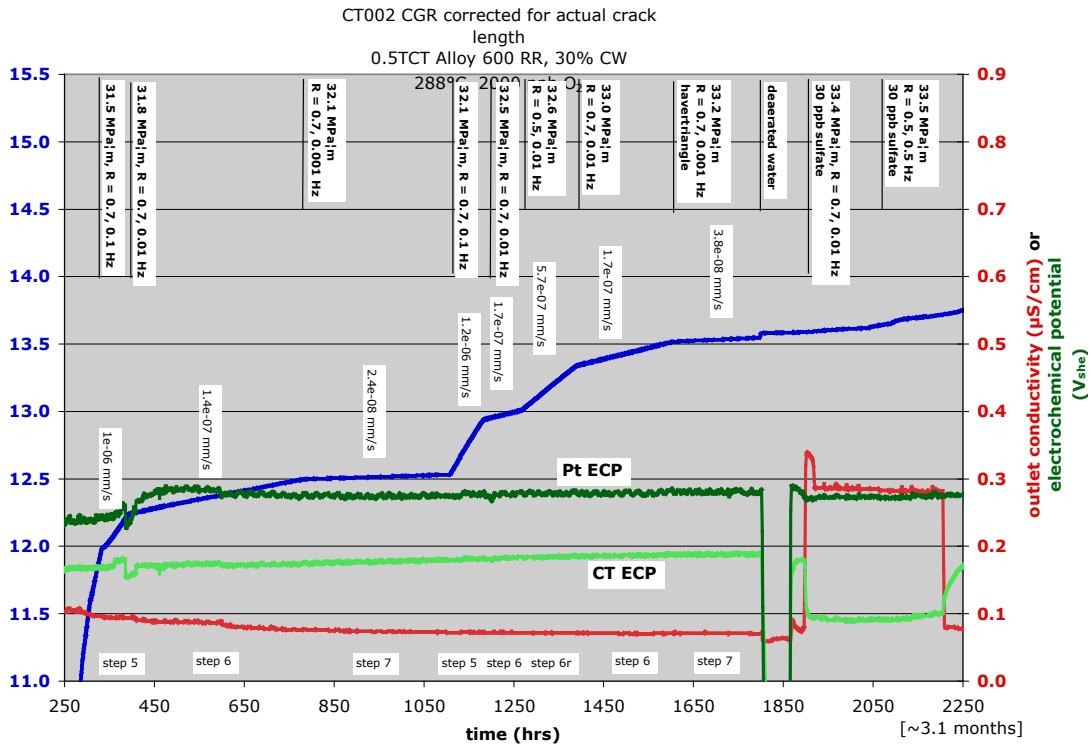


Figure 4-13 In-situ Pre-Cracking and Crack Transitioning Steps for Alloy 600 Test



**Figure 4-14 Alloy 600 CGR Test Results Following Round-Robin Prescribed Steps**

stringers. It was decided that several subsequent steps should be applied to this sample to confirm the cracking characteristics. The first was to remove oxygen from the feedwater and monitor the change in electrochemical potential. An immediate drop in ECP was measured on the sample and on the Pt electrode at ~1800 h when deaerated conditions were established, and then the ECPs returned to the previous high values when oxygen was again added to the system. In a final attempt to coax SCC, 30 ppb sulfate was added as an impurity to the oxidizing BWR water environment at ~1890 h. The small  $H_2SO_4$  addition (at  $R=0.7$  and  $f=0.01$  Hz) caused a small drop in ECP on the CT sample from 0.2 to 0.1  $V_{she}$ . Over a period of 200 h, the sulfate did not accelerate the CGR beyond that of the sluggish rate of the non-sulfate condition (see step 6 for the non-sulfate CGR).

In an attempt to promote more rapid crack advance, the R ratio was changed to 0.5 and the frequency was increased to 0.5 Hz at ~2080 h. However, no increase in growth rate was observed. All results for this test raised concerns for this alloy 600 material. Due to the extensive length of this test and known problems with this heat of alloy 600, the decision was made to terminate this test and move forward on another aspect of the capability demonstration sequence. Fatigue cycling in air was employed to fracture the alloy 600 sample for subsequent surface examinations to investigate the cracking morphology and calibrate the dcpd measurements of crack length. An overview of the sample fracture surface is presented in Figure 4.15. Slow crack growth was experienced over the nearly 4-month test time and alloy 600 microstructural problems are suggested by the torturous appearance at crack depths from ~1.5 to 3 mm measured from the crack notch (see arrows in micrograph).

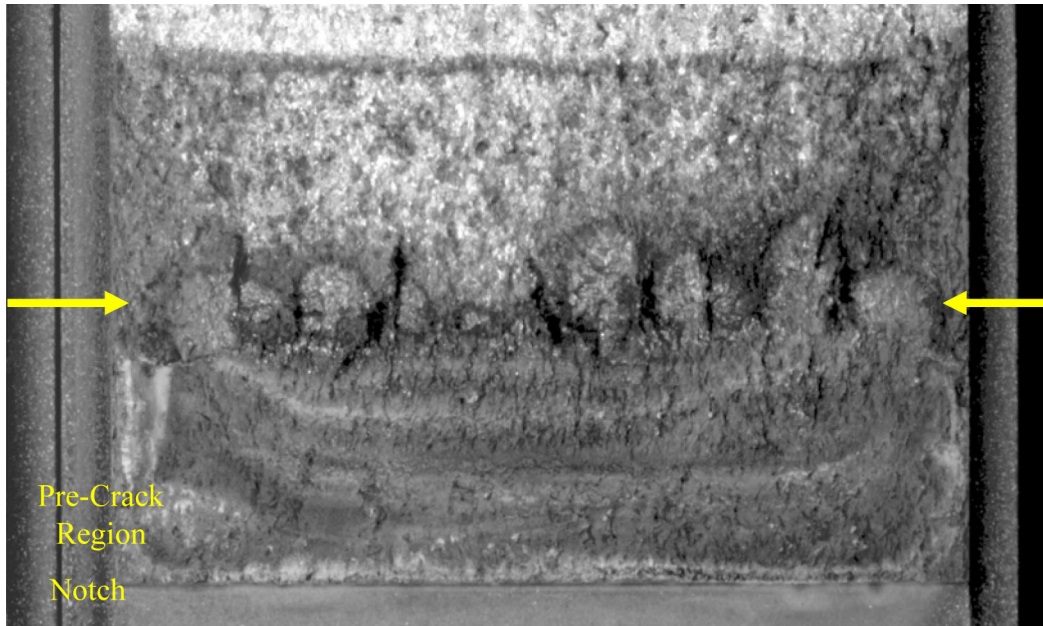


**Figure 4-15 Optical Micrograph Showing Fracture Surface for Alloy 600 Round-Round Sample (CT002) tested in Simulated BWR Oxidizing Water with 30 ppb Sulfate Added**

SEM examinations of the alloy 600 round-robin test sample fracture surface were performed and comparisons were made to the dcpd measurements of crack extension. The fracture surface shown in Figure 4.15 documents a reasonably straight crack front and a total average crack length of 17.1 mm. The dcpd system underpredicted the actual crack length with an estimated value 15.4 mm.

The next validation test evaluated a 0.5T CT, alloy 182 weld metal sample from a second ICG-EAC round robin with the test performed in high-purity oxidizing BWR water (2000 ppb  $O_2$ ). Crack-transitioning steps were initiated at ~45 h with a load ratio of 0.7 and cycling at a frequency of 0.1 Hz as shown in Figure 4.16. The cyclic frequency was then decreased to 0.01 Hz and a crack-growth rate established of  $\sim 2.1 \times 10^{-7}$  mm/s before decreasing the frequency further to 0.001 Hz with a haversine loading form at 220 h. SCC response was evaluated in high-purity water until a test time of ~650 h. Crack growth rates were extremely low even with the load cycling, so 30 ppb sulfate was added to solution. As expected, the growth rate increased after sulfate addition and the test was converted to constant K at ~900 h. Under constant K conditions, a stable growth rate of  $\sim 3$  to  $4 \times 10^{-7}$  mm/s in sulfate was observed over a period of ~850 h (34 d) as shown in Figure 4.17. As per the round-robin instructions, a fatigue cycle (helping ensure that the crack front was straight) was applied at ~1780 h and then constant K conditions were briefly re-established before the test was ended at ~2000 h.

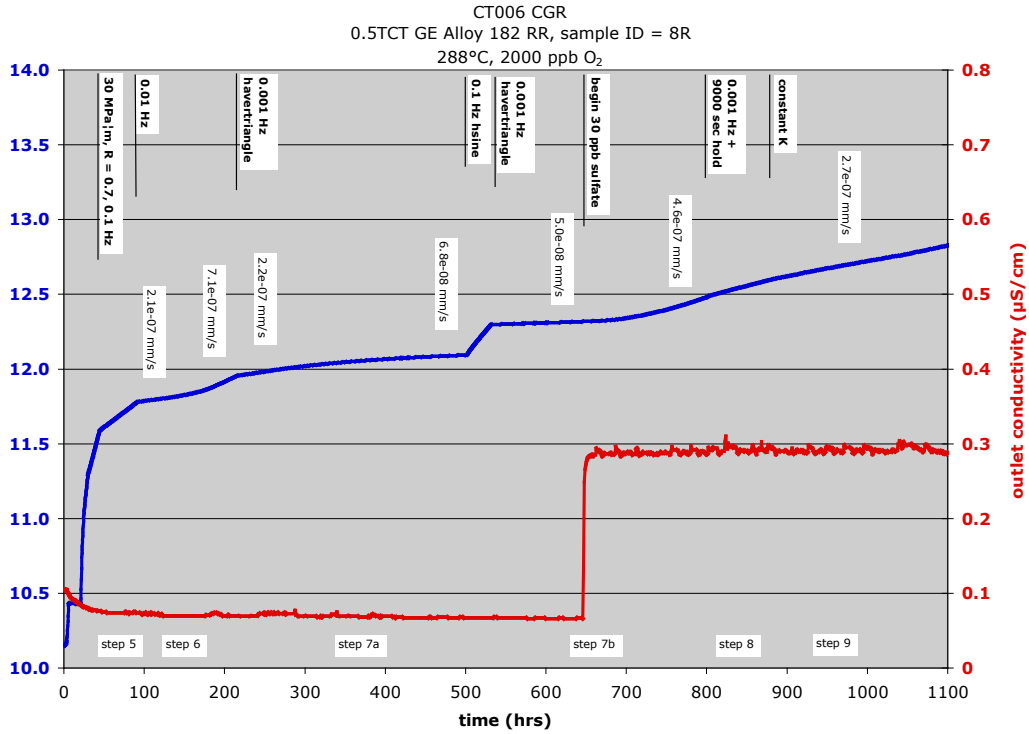


**Figure 4-16 Pre-Cracking and Transitioning Stages for Alloy 182 Test in BWR Oxidizing Water**

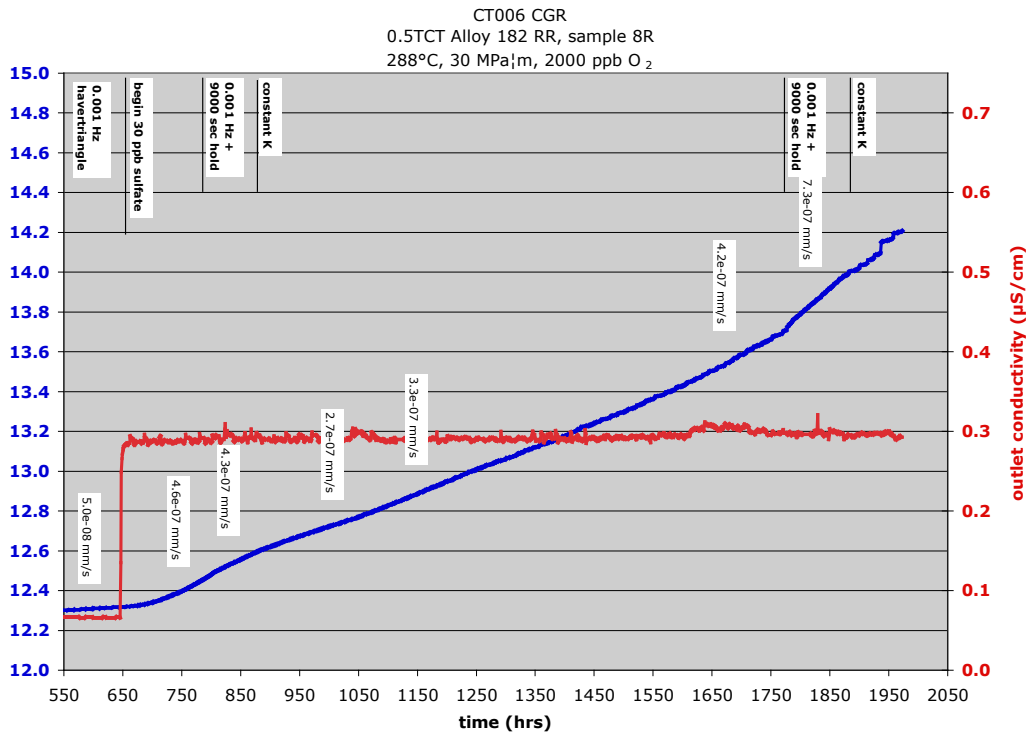


**Figure 4-17 Crack-Growth Response for Alloy 182 in BWR Oxidizing Water During Steps Under Constant K and then with Cyclic Loading with a Hold Time.**

Crack-growth-rate testing was also initiated on the alloy 182, 0.5T CT sample from the ICG-EAC round robin in PWR water. The test conditions are 325°C (617°F), 1000 ppm B, 2.0 ppm Li, 29 cc/kg H<sub>2</sub>, and a stress intensity of 30 MPa√m (27.3 ksi√in). This represented our first test in PWR-simulated water and at temperatures greater than 290°C (554°F). A reasonable learning curve was required to establish and maintain the target PWR primary water, B and Li chemistry. Several minor B/Li additions were needed and are reflected in the reductions in outlet conductivity. The gradual increase in water conductivity that occurs from ~100 h to 430 h is due to Fe<sup>++</sup> and chromate displacing Li<sup>+</sup> in the demineralizer. At 430 h, auto injection of Li-free water was established to automatically control B/Li levels during a test. Initial pre-cracking phases (following the round-robin procedure) were conducted leading up to the cycling at 0.01 Hz. Crack growth behavior during initial pre-cracking and crack transitioning steps is shown in Figure 4.18. Cyclic loading at 0.01 Hz produced a crack-growth rate of  $\sim 2 \times 10^{-7}$  mm/s. The cyclic loading rate was decreased to 0.001 Hz at ~370 hours and a significant decrease in growth rate was observed reaching a stable rate of  $\sim 5 \times 10^{-8}$  mm/s. A final SCC transitioning step with a 9000 second hold time further decreased the measured propagation rate to  $\sim 1 \times 10^{-8}$  mm/s.

At 1510 h, the final stage of the round-robin procedure was applied by going to constant K conditions. Test behavior under constant K conditions is shown in Figure 4.19. No crack growth was detected over the first ~300 h, but then a stable propagation rate of  $\sim 2 \times 10^{-9}$  mm/s was observed over the next ~600 hours. PNNL results are consistent with experience of other

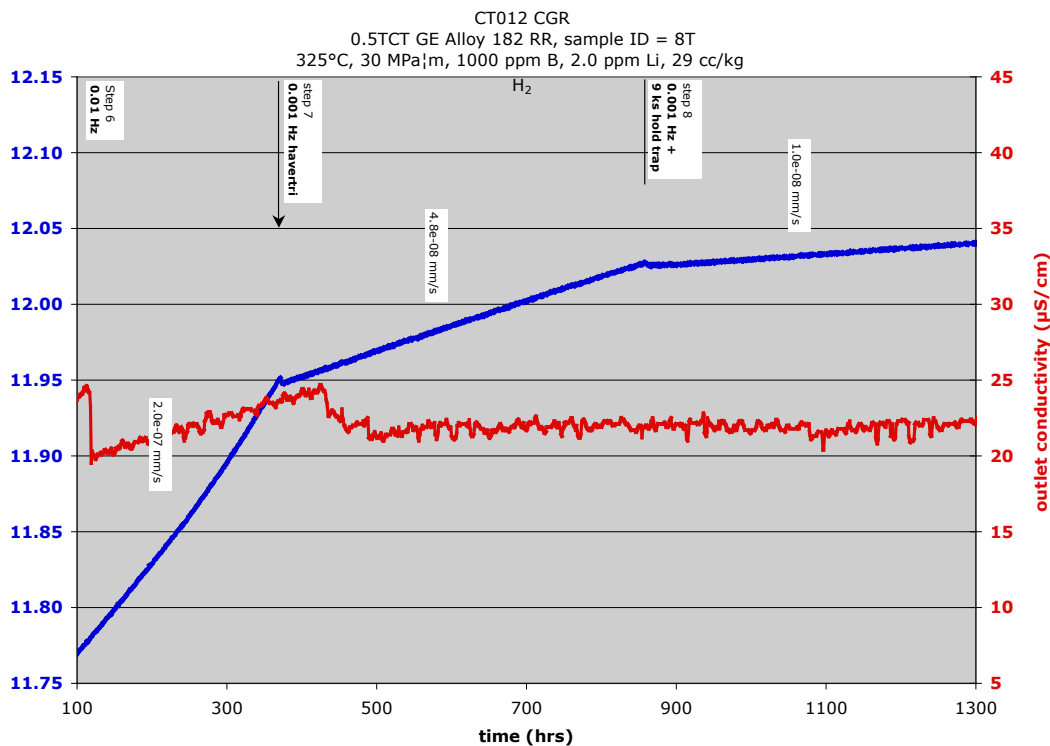


**Figure 4-18 Crack Transitioning Stages for Alloy 182 Round Robin Test in PWR-Simulated Primary Water at 325°C (617°F).**

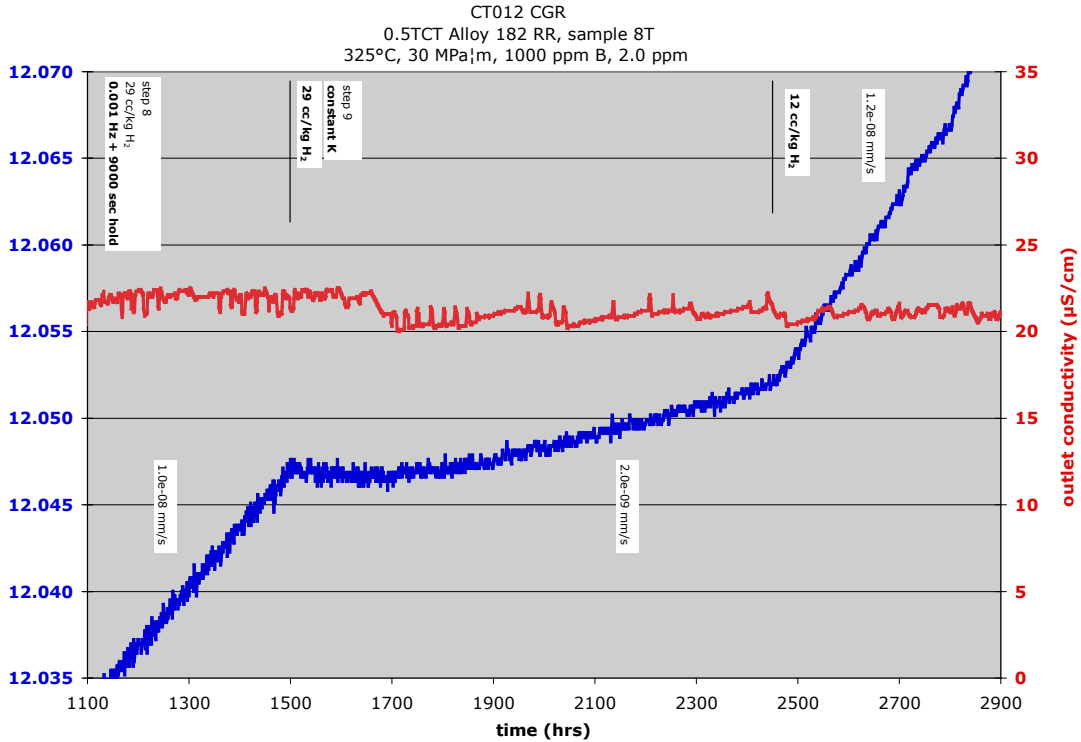


**Figure 4-19 Hydrogen Effects on SCC CGR of Alloy 182 under Constant K Conditions**

key laboratories participating in the ICG-EAC round robin and complete our various round-robin tests to demonstrate and validate our test capabilities. After completion of the round-robin obligation, it was decided to briefly examine the effect of H<sub>2</sub> concentration on the SCC response by decreasing the hydrogen content to 12 cc/kg. Based on extensive work at Knolls Atomic Power Laboratory (KAPL), this concentration should give a pH/potential close to the Ni/NiO transition line and increase susceptibility to SCC crack growth. The response to this change was immediate, and the propagation rate has increased by ~6X to  $\sim 1.2 \times 10^{-8}$  mm/s consistent with the reported increases by KAPL of 5-8X for alloy 182 weld metal. As there is very little data in the literature on this H<sub>2</sub>/ECP effect, crack-growth response is being evaluated at even lower H<sub>2</sub> levels (5 cc/kg H<sub>2</sub> and 1.5 cc/kg H<sub>2</sub>) as part of ongoing testing.

As much as was possible, the PNNL-generated BWR and PWR alloy 182 round robin results were compared with that of the other participating laboratories. Fourteen other laboratories presented information at the 2005 and 2006 ICG-EAC meetings on this alloy 182 material. These results were summarized in a presentation by Martin Morra of GEG at the 2006 meeting. Only two labs, Studsvik and PNNL, have tested under both BWR and PWR conditions. Six other labs tested in BWR water: GEG, NRI-REV, VTT, AREVA (Germany), Toshiba, and PSI. Six different labs performed experiments only in PWR water: SCK-CEN, CEA, EdF, CIEMAT, Serco, and ANL. The general conclusions were that this alloy 182 heat was not highly prone to SCC propagation, sulfate additions increased growth rates in BWR water, and SCC propagation was very difficult in PWR water. Many organizations could not generate reproducible crack-growth data for comparison under the specified round-robin conditions, and considerable scatter

was observed among the different labs. A key issue affecting comparisons was that some laboratories deviated from the specified round-robin test recipe. There were deviations in both the pre-cracking steps and in the length of time at constant K. As a result, the extent of IGSCC engagement from the TG fatigue pre-crack may have been markedly different among labs. The resulting variation in crack growth rate between labs provides more evidence for the need to have careful and systematic transitioning steps with reduced cycle frequencies and increased hold times when trying to establish stable SCC propagation.

Another important issue was variations in equipment among the participants. Only a few labs obtained in-situ measurements of crack extension by dcpd with some of those labs having considerable scatter in their dcpd values making it difficult to determine a crack growth rate in this crack growth-resistant material. Some labs lacked the ability to maintain constant K levels during the test, while others did not perform their constant K tests at the specified K value of  $30 \text{ MPa}\sqrt{\text{m}}$  ( $27.3 \text{ ksi}\sqrt{\text{in}}$ ).

In light of these limitations, the best that can be done for comparing CGR rates among the participants is to compare specific round-robin step conditions for labs that kept reasonable K levels, had minimal data scatter, and had sufficient hold times at the conditions of interest. Four labs reported propagation rates for the 0.001 Hz cycling in BWR oxidizing water with a K of 27 to  $31 \text{ MPa}\sqrt{\text{m}}$  ( $24.4$  to  $28.1 \text{ ksi}\sqrt{\text{in}}$ ). These growth rates ranged from 0.9 to  $9 \times 10^{-8} \text{ mm/s}$  with PNNL's result of  $5$  to  $7 \times 10^{-8} \text{ mm/s}$  being squarely in the middle of that range. For a constant K of  $30 \text{ MPa}\sqrt{\text{m}}$  (steps 9 and 11), three propagation rates were reported in BWR oxidizing water with 30 ppb sulfate. The rates with sulfate ranged from 1.5 to  $9 \times 10^{-7} \text{ mm/s}$ . The value observed in testing at PNNL was  $3$  to  $4 \times 10^{-7} \text{ mm/s}$ , again consistent with the data from the other labs.

Less overall data were available from the participating laboratories under  $325^\circ\text{C}$  ( $617^\circ\text{F}$ ) PWR conditions, but most were performed at K levels similar to what was requested by the round robin. For the 0.001 Hz cycle with K ranging from  $\sim 29$  to  $32 \text{ MPa}\sqrt{\text{m}}$ , PNNL measured a rate of  $4.8 \times 10^{-8} \text{ mm/s}$ , which is consistent with three labs reporting growth rates ranging from 0.2 to  $2 \times 10^{-7} \text{ mm/s}$ . PNNL's rate with the 9000 s hold time was  $1 \times 10^{-8} \text{ mm/s}$ , which is also consistent with three other labs reporting rates ranging from 0.9 to  $9 \times 10^{-8} \text{ mm/s}$ . Finally, four labs reported constant K ( $\sim 29$  to  $35 \text{ MPa}\sqrt{\text{m}}$ ) CGR rates of  $\sim 0.7$  to  $3 \times 10^{-8} \text{ mm/s}$ , while our results in Figure 4.19 indicate a slower rate of  $2 \times 10^{-9} \text{ mm/s}$ . While the PNNL rate is below that of the other labs, the rate has been reproduced several times during ongoing testing of this sample, and it has been determined that this material is sensitive to the amount of dissolved hydrogen with the CGR increasing to  $1 \times 10^{-8} \text{ mm/s}$  at  $12 \text{ cc/kg H}_2$ . Overall, PNNL has successfully demonstrated that our CGR testing capabilities match or exceed those in other organizations.



## 5 SCC Crack-Growth-Rate Testing of Alloy 690 and Its Weld Metals

### 5.1 Materials

Multiple heats of alloy 690 CRDM tubing from Vallourec were purchased and received at PNNL in February 2005. This shipment included five tubes with each tube made from a different heat, plus two tubes of different wall thicknesses made from a sixth heat. All tubing pieces were obtained in ~2 ft lengths with each tube having sufficient wall thickness for 0.5T CT samples in several possible orientations. Alloy 690 plate and an alloy 152 mockup weld were also obtained from EPRI. The materials are summarized in Table 5.1, and several of the alloy 690 CRDM tubing sections are shown in Figure 5.1 after receipt at PNNL.

Selected PWR CRDM materials were also received in April 2005 from AREVA in Chinon. Four alloy 690 components included: (1) a sleeve (no honing) from a U.S. reactor vessel closure head (RVCH), Westinghouse design; (2) an adaptor (with honing) from a U.S. RVCH, Westinghouse design; (3) an adaptor (with honing) from EDF RVCH; and (4) an adaptor (with honing) from U.S. RVCH, B&W design.

**Table 5-1 Alloy 690 and 152 Test Materials**

Material - Source	Heat No. and Description	Composition, wt%
Alloy 690TT – Valinox	RE076, CRDM Tube 2146 (1.1 in. wall)	Ni-29Cr, 10.1Fe, 0.019C (full analysis not available)
Alloy 690TT – Valinox	RE169, CRDM Tube 2175 (1.0 in. wall)	Ni-29.4Cr, 10.3Fe, 0.020C (full analysis not available)
Alloy 690TT – Valinox	RE243, CRDM Tube 2216 (1.0 in. wall), Tube 2360 (1.4 in. wall)	Ni-28.9Cr-10.4Fe-0.02C-0.3Mn- 0.35Si-0.14Al-0.23Ti, <0.001S
Alloy 690TT – Valinox	WP016, CRDM Tube 2422 (1.1 in. wall)	Ni-29.3Cr, 10.3Fe, 0.020C- 0.32Mn- 0.27Si-0.16Al-0.25Ti, <0.0005S
Alloy 690TT – Valinox	WP140, CRDM Tube 2502 (1.2 in. wall)	Ni-29.0Cr-10.4Fe-0.03C-0.3Mn- 0.33Si-0.18Al-0.3Ti, <0.001S
Alloy 690TT – Valinox	WP142, CRDM Tube 2541 (1.2 in. wall)	Ni-29.0Cr-10.5Fe-0.02C-0.3Mn- 0.35Si-0.18Al-0.27Ti, <0.001S
Alloy 690TT – EPRI <sup>(a)</sup>	NX8625HG21, 1.34 in. Plate	Ni-30Cr, 10Fe, 0.027C (full analysis not available)
Alloy 152 – EPRI	Mock-up weld by MHI <sup>(b)</sup>	Ni-28.7Cr-9.1Fe-0.03C-3.6Mn, 0.33Si-0.15Al-0.12Ti-0.003S
(a) EPRI = Electric Power Research Institute		
(b) Mitsubishi Heavy Industries		



**Figure 5-1 Four of the Alloy 690 CRDM Tubes Received at PNNL**

Initial 690/152 material analysis and testing started with the alloy 152 mockup weld obtained from EPRI. The mockup weld was produced for the Kewaunee pressure vessel head replacement by MHI. It was made using 2.4-in. thick plates of 304SS butted together and with a u-groove across the butt cross section. Alloy 152 butter passes were applied, and then the plates were welded together with alloy 152. A portion of the weldment was sectioned at PNNL into 0.75-in.-thick blocks (Figure 5.2) and metallographically prepared to reveal the individual weld passes and the butter zone. Sections C, D, and E indicated in Figure 5.2 were selected for fabricating CT samples. These samples were marked for machining so as to locate the end of the pre-crack in a single weld pass and enable >1 mm of growth in that weld pass. A close examination was made to select a weld pass where the dendrites would be parallel to the pre-crack. The machined notch in section C is shown in Figure 5.3. Crack growth testing will take place in the weld pass below the pass where the machined notch is located. The pre-crack will end in the same weld pass for sections C and D, but the slight wandering of the welds along the length of the mockup meant that it was necessary to use a different weld pass for crack growth testing (moving one up) of section E.

Characterizations of the alloy 690 and alloy 152 materials are described in Sections 6.2 and 6.3, respectively. These characterizations include basic microstructure and microchemistry of the as-received materials for materials with selective heat treatments that have been performed to-date.

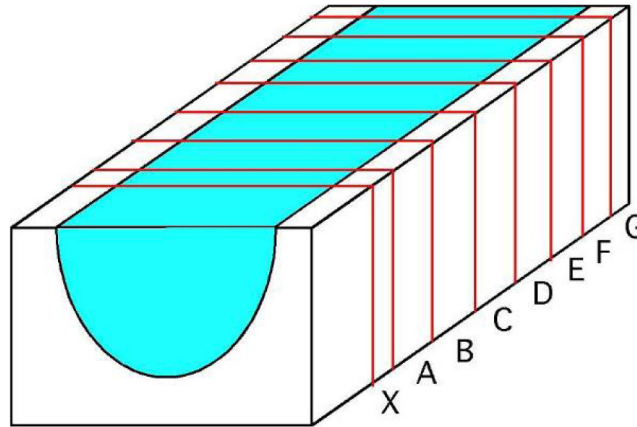


**Figure 5-2 Sectioning Diagram for the 152 Welded Block. End sections X and G are 0.5-in. thick and are used for metallographic observations while sections A-F are 0.75-in. thick and are to be used for CT samples. There is approximately 3 in. of welded block in front of section “X”.**

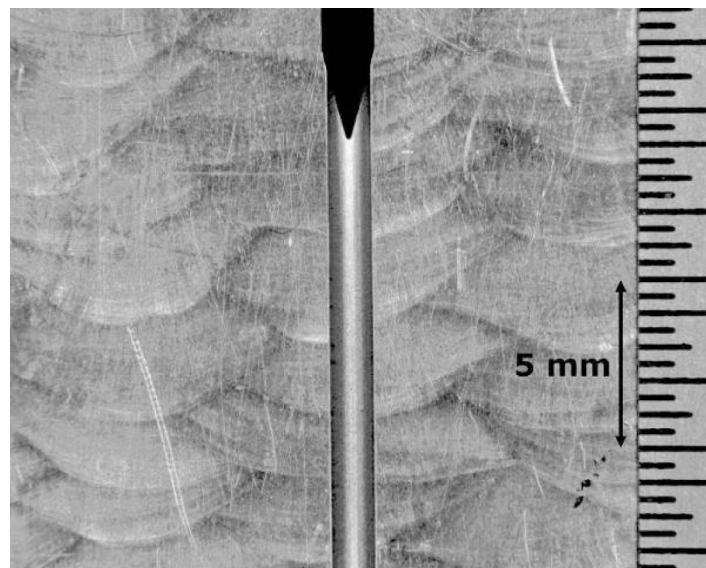


**Figure 5-3 Optical Micrograph of Section C Showing the Location of the Machined Notch. This same weld pass was selected in section D, while the one just above and to the left was selected in section E.**

## 5.2 Alloy 152 Crack-Growth Testing

The first alloy 152 weld metal test (from the MHI mock-up weld) was set up in NRC System #1 using PWR water chemistry identical to that used for the alloy 182 round robin test. A pre-cracking process similar to that for the 182 round robin (RR) has also been adopted with a target K value of  $30 \text{ MPa}\sqrt{\text{m}}$  ( $27.3 \text{ ksi}\sqrt{\text{in}}$ ) for constant K testing. The pre-crack increments on the 0.5T CT sample are shown in the weld macro in Figure 5.4.

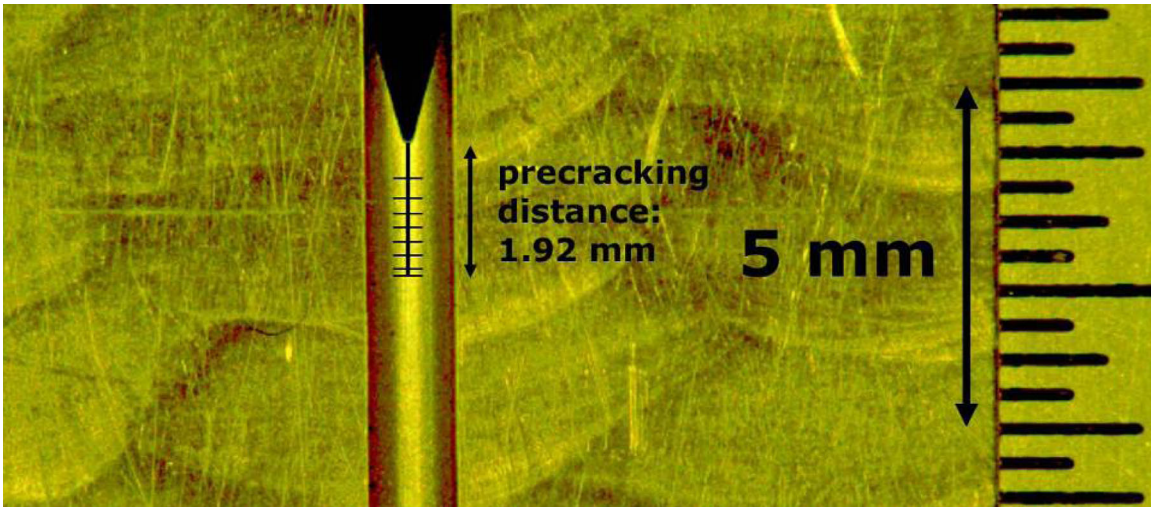


**Figure 5-4 Intended Pre-Crack Increments for CT013 Alloy 152 MHI Mock-Up Weld Crack-Growth Test Being Conducted in NRC System #1**

The pre-crack was grown to ~1.3 mm in fatigue over the first 25 h so that crack-growth testing would begin in the middle of a weld pass. Crack transitioning from fatigue to corrosion fatigue was then continued through the next three steps cycling first at 0.01 Hz for ~0.2 mm of crack growth giving a rate of  $\sim 3.5 \times 10^{-7}$  mm/s which was followed by cycling at 0.001 Hz for ~0.1 mm giving a rate of  $5.4 \times 10^{-8}$  mm/s. The last transition step of 0.001 Hz with a 9000 s hold was intended to run for 0.1 mm, but the low crack growth rate of  $6.8 \times 10^{-9}$  mm/s dictated an increment of only 0.01 mm (taking approximately 3 weeks). The steps are documented in Figures 5.5 and 5.6. Because of the extremely slow, but stable propagation rate at the 9000s hold time, a longer hold time of 86,400 s (24 h) was selected as a final crack transitioning step to constant K. An apparent near-stable CGR of  $\sim 1.6 \times 10^{-9}$  mm/s was measured during the first 2.5 weeks in this test condition. However, the dcpcd-measured extension has been less than 2  $\mu\text{m}$  as illustrated in Figure 5.7. Plans are for this test to continue for several more months attempting to establish SCC crack-growth rates in alloy 152 under constant K, and perhaps under several gentle cycling conditions. We anticipate investigating the influence of temperature and hydrogen level on the SCC response. It is possible that temperatures up to  $\sim 340^\circ\text{C}$  ( $644^\circ\text{F}$ ) will be evaluated and temperatures down to  $\sim 100^\circ\text{C}$  ( $212^\circ\text{F}$ ) may be examined at the end of this test.

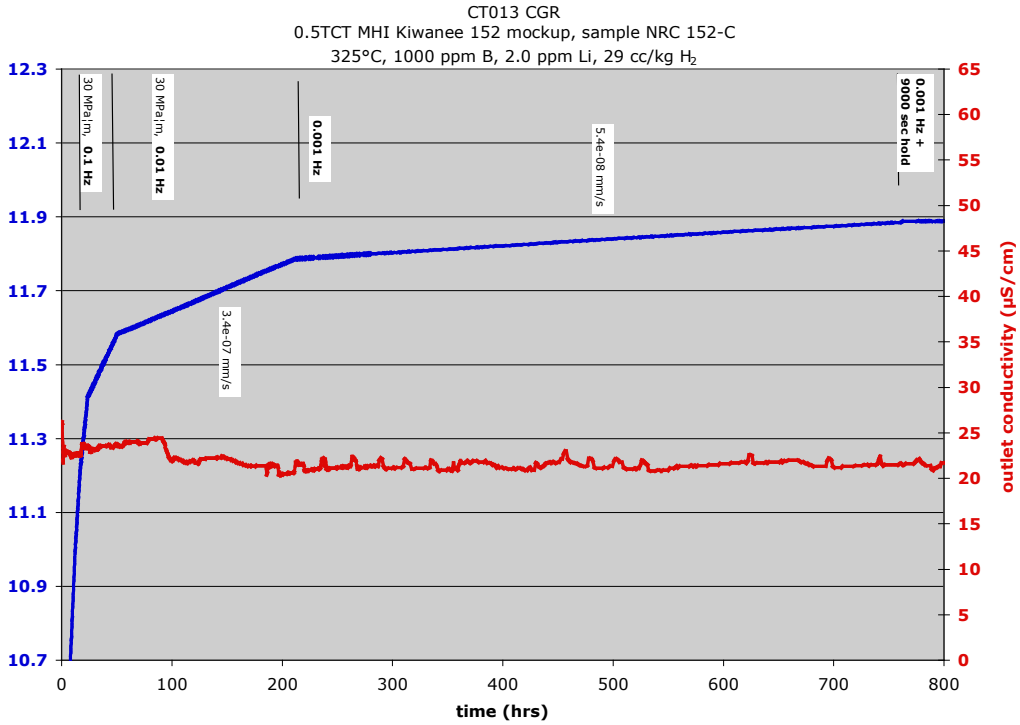


**Figure 5-5 Pre-Cracking and Initial Crack Transitioning for the First Alloy 152 CGR Test in PWR-Simulated Primary Water at 325°C (617°F).**

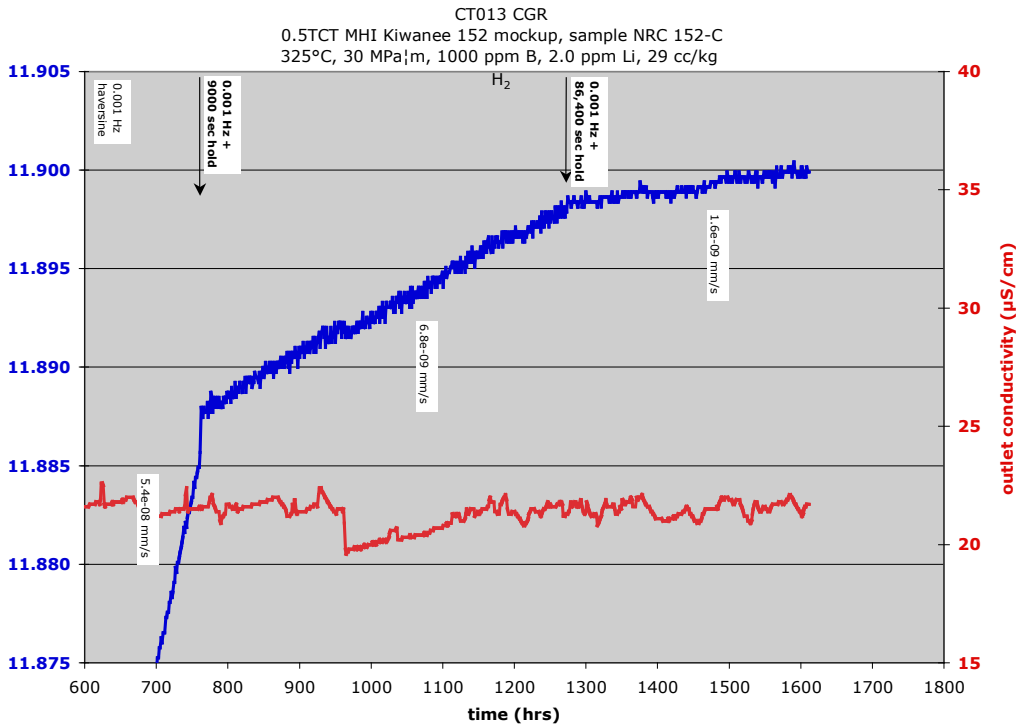


**Figure 5-6 Crack Transitioning for the First Alloy 152 CGR Test in PWR-Simulated Primary Water at 325°C (617°F).**

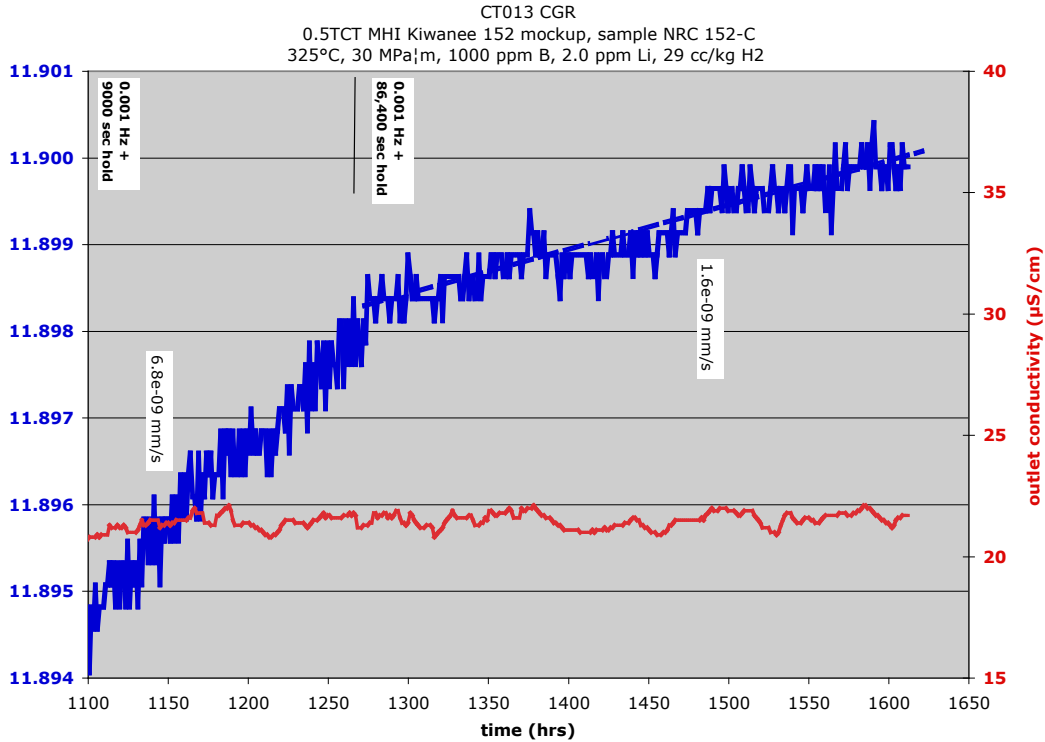


**Figure 5-7 Expanded View of Final Crack Transitioning Step in the First Alloy 152 Test. The test is on-going.**

### 5.3 Alloy 690 Crack-Growth Testing

The first machined alloy 690 samples were pre-cracked and CGR testing started shortly before this report was prepared. Initial progress on this important test is briefly summarized here. However, as with the alloy 152 test in the previous section, most data will be provided in future reports.

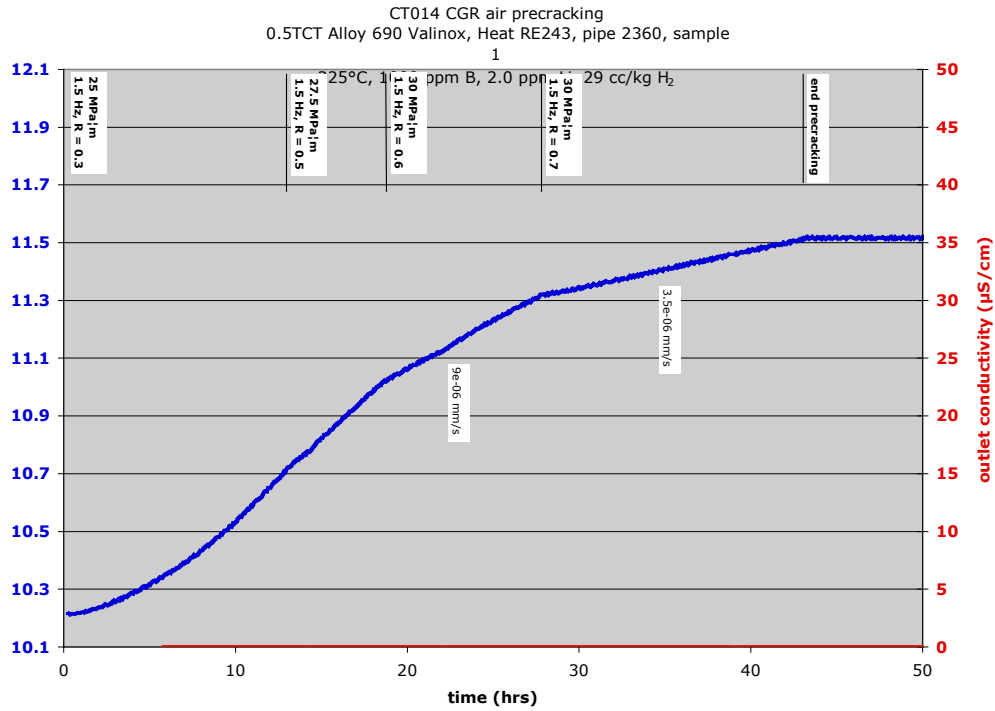
Microstructural characterizations (see Section 6.3) revealed no significant variations in grain size or precipitate structures for the six separate CRDM alloy 690TT tube heats. Heat RE243 was selected for these initial tests because it was available in two different product sizes and provides excess material for future testing in different material conditions. The decision was made to test the first alloy 690 samples in series and examine the influence of a solution-anneal (SA) heat treatment (1100°C/2012°F for 1h and water quench) on CGR response. The anneal was given to the sample after it had been machined into a 0.5T CT. This treatment was found to make only a minor change in the material grain size, but did remove most chromium carbides from grain boundaries in comparison to the as-received TT condition. Somewhat surprisingly, a significant decrease (~25%) in hardness was observed for the SA sample. Because the CRDM tube was thermally treated, it was anticipated that this anneal would have a much smaller effect on strength.



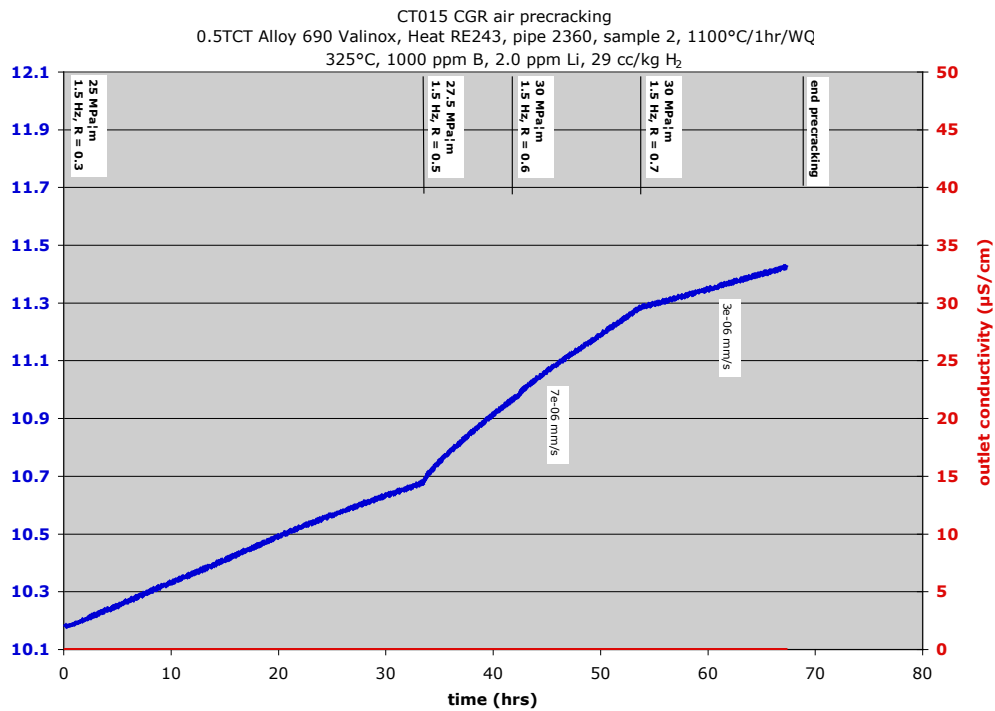
**Figure 5-8 Image Showing the Two Alloy 690, 0.5T CT Samples Mounted in Series Within SCC CGR Test System #3**

In order to test these samples in series (as illustrated in Figure 5.8), it was necessary to pre-crack each of these samples (CT014 and CT015) in air prior to loading the samples into the autoclave. A difference in initial fatigue response was observed for the two alloy 690 samples. This is shown in Figure 5.9 with the SA alloy 690 (b) exhibiting an unexpected linear response with initial aggressive cycling, while the as-received alloy 690TT (a) revealed the more typical increasing response. The later air-fatigue steps, however, gave a similar pre-crack characteristic. After pre-cracking, the samples were mounted into the high-temperature autoclave.

As noted earlier, the SCC CGR test on these two samples in series was just initiated at the time of this report. The first stage of the crack transitioning sequence is shown in Figure 5.10 for the CT014 (CRDM alloy 690 in the thermally treated condition) and CT015 (SA alloy 690) samples. The measured CGRs are consistent between the two samples, but are somewhat lower than expected based on our alloy 152 results and isolated alloy 690 results available from other laboratories. At the current test step of 0.1 Hz, the cracks in these two 690 samples are growing at  $4.4 \times 10^{-7}$  mm/s, while for the alloy 152 sample, the CGR was  $1.6 \times 10^{-6}$  mm/s which is over an order of magnitude higher than the 690 samples. This would seem to suggest very low crack growth rates later in the test, but it is too early in this test for any meaningful assessments of the alloy 690 crack-growth rates to be made. The only purpose of presenting this early data is to document that our tests on alloy 690 and alloy 152 are underway after the successful construction, demonstration, and validation of the PNNL test systems and CGR testing capabilities.



(a)



(b)

**Figure 5-9 Air Fatigue Pre-Cracking of Alloy 690 Samples to be Tested in Series: (a) as-received CRDM material in TT condition (CT014) and (b) solution-annealed material (CT015).**

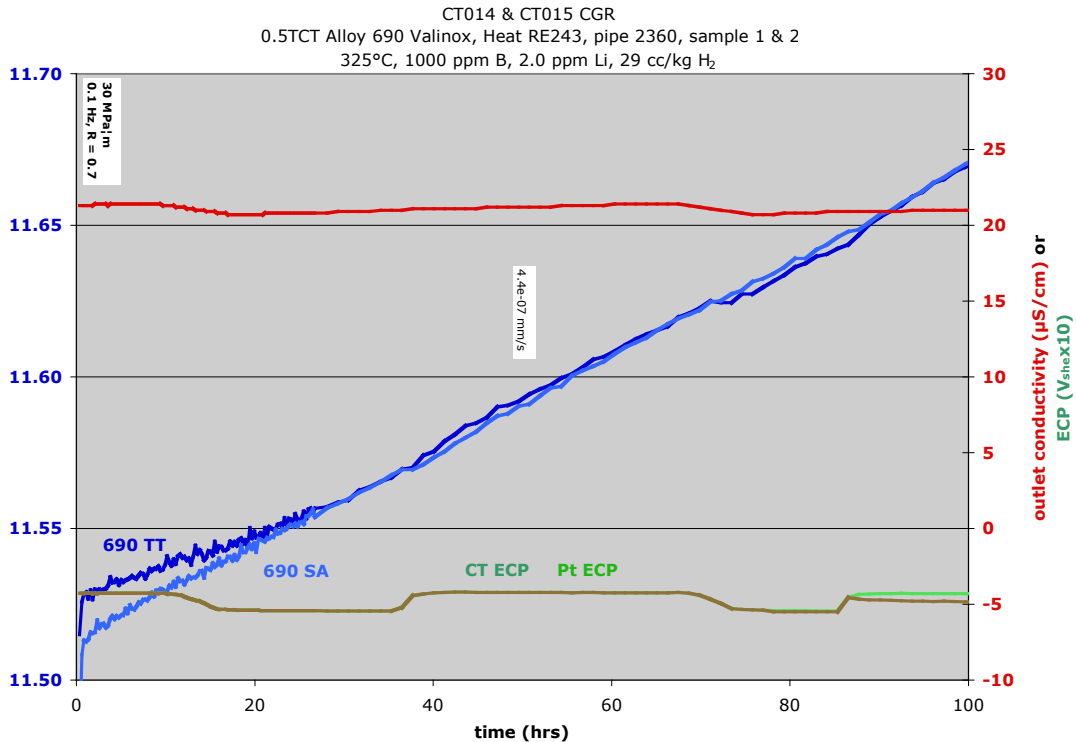


**Figure 5-10 Initial Crack Transitioning Step for Alloy 690 Samples Tested in Series**

## 5.4 Plans for Future Testing

Plans are to test alloy 690 after specific thermomechanical treatments that will include heat treatments to alter initial microstructures and simulate heat-affected-zone characteristics plus cold rolling or forging to increase strength levels. Further tests on alloy 152 may also be performed after applying selected treatments, and we will also examine weld-to-pipe transition zones. Samples will be tested under a variety of environmental conditions including different temperatures, B/Li concentrations, and hydrogen overpressures. When requested by the NRC, tests will be performed on alloy 600 and 182 samples taken from in-service components. Tests may also be performed on samples made from hot-cracked weld material as possible. With the 9–12 month long tests required for the alloy 690 and 152 materials and having only three crack-growth systems at our disposal, it will be impossible to perform multiple tests at all material and environmental conditions of interest. Examination of the available data in the literature and limited SCC scoping studies will be performed to determine the most pertinent conditions. Tests will start with those conditions that are believed to promote SCC susceptibility. Some of the known or probable means for achieving higher crack growth rates in alloy 690 and 152 are discussed briefly below.

While one means to maximize the CGR is to go to higher K values, there is also the necessity to stay within the  $K_{IEAC}$  validity range and have a common basis of comparison for all materials/conditions evaluated. Based on available strength data of alloy 690 and 152 in various conditions, an appropriate K value is  $30 \text{ MPa}\sqrt{\text{m}}$  ( $27.3 \text{ ksi}\sqrt{\text{in}}$ ). Perhaps in selected instances,

the effect of higher K values will be studied after first obtaining data at the reference value of 30 MPa√m. The maximum applied value will depend on the strength of the material being tested.

Literature data on alloy 600 and its weld metals show that crack-growth rates increase with test temperature and can be influenced by hydrogen overpressure. However, similar dependence has not been established for alloy 690 or its weld metals. Different mechanistic processes may control SCC in the lower Cr alloy 600 materials than in the higher Cr alloy 690 materials. Effects of these important environmental variables will be studied on the more resistant alloys including test temperatures up to 360°C (680°F) at modified hydrogen concentrations. In addition, it is anticipated that isolated tests will be conducted to evaluate possible enhanced cracking at low temperatures (~100°C) and with minor solution impurities.

Very recent presentations from Bettis on alloy 690 SCC testing has revealed that the material may have much higher crack growth rates when the material is cold rolled and tested with the crack plane parallel to the rolling direction (S-L orientation). Attempts will be made to reproduce and investigate this effect. The propagation rate in this condition will be compared with the crack-growth rate for other cold-worked or cold-forged conditions to isolate the influence of matrix strength and microstructure on SCC. At a minimum, the higher-strength alloy 690 materials will be examined in heat-treated conditions to alter grain boundary carbide precipitation.

## 6 Materials Characterization

### 6.1 Alloy 182 Weld Metal

Microstructural and microchemical characterization was performed on the alloy 182 weld metal obtained as part of the ICG-EAC round robin (CT006 and CT012). Optical metallography, SEM, and TEM were used to document the general grain structures, identify precipitates and inclusions, and assess local compositional variations. Most regions showed large and elongated grains as illustrated in Figure 6.1. A distribution of large and small second-phase particles were present as indicated by the light or dark contrast features in the SEM backscatter image in Figure 6.2. Boundaries often had a crenulated appearance due to IG carbides.

Higher-magnification TEM examinations revealed a high dislocation density in most grains along with micrometer-sized carbides in the matrix and at grain boundaries as presented in Figure 6.3. A high density of much smaller, nanometer-sized  $M_{23}C_6$  and MC carbides were also found at most grain boundaries. An example of these fine precipitates is shown by the darkfield images in Figure 6.4. Nanometer-scale measurements of grain boundary composition between  $M_{23}C_6$  carbides indicated strong Cr depletion with levels down to ~5 wt% (matrix 13–15 wt%).

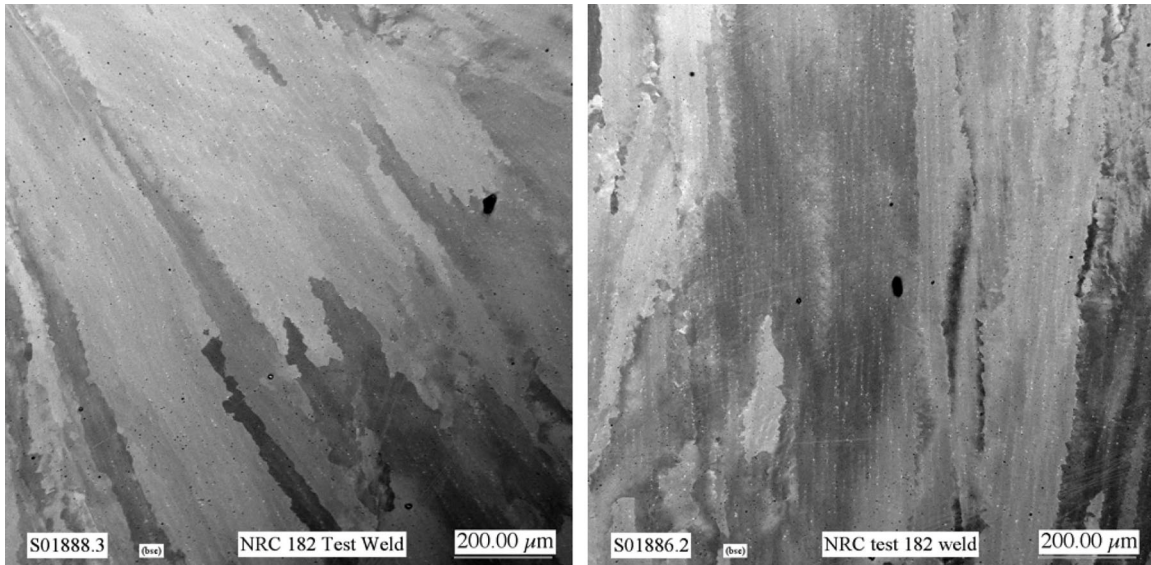


**Figure 6-1 SEM Backscatter Electron Images Showing Elongated Grain Structure in the Round-Robin Alloy 182 Weld Metal.**

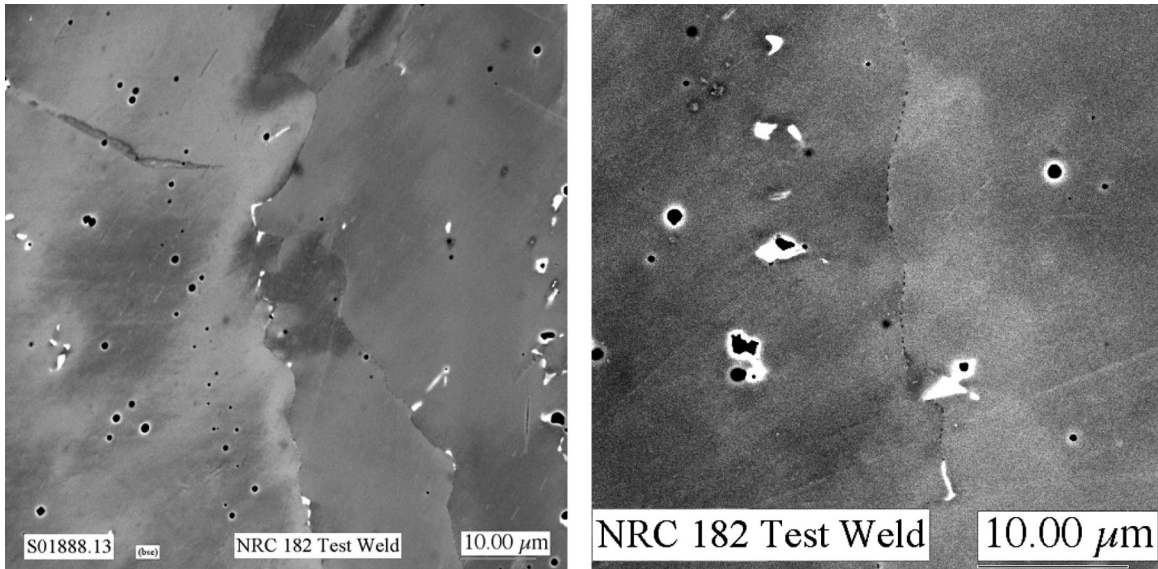


**Figure 6-2 SEM Backscatter Electron Images Showing “Crenulated” Boundaries Caused by Presence of Carbide Precipitates.**

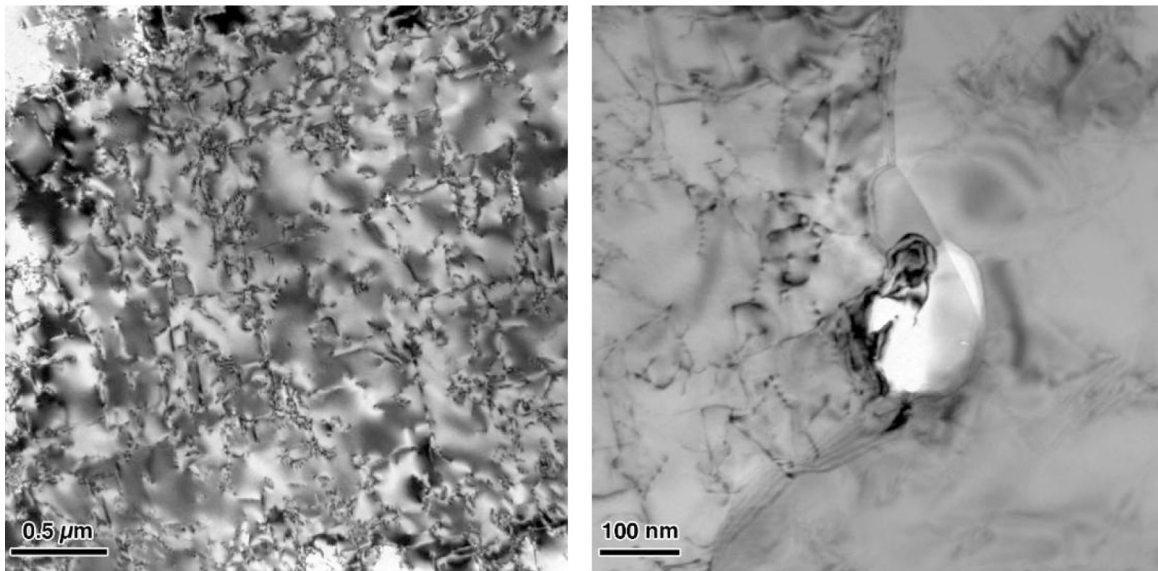


**Figure 6-3 TEM Brightfield Images Illustrating High Dislocation Densities in Most Regions (left) and  $M_{23}C_6$  and MC Carbides in the Matrix and at Grain Boundaries (right).**

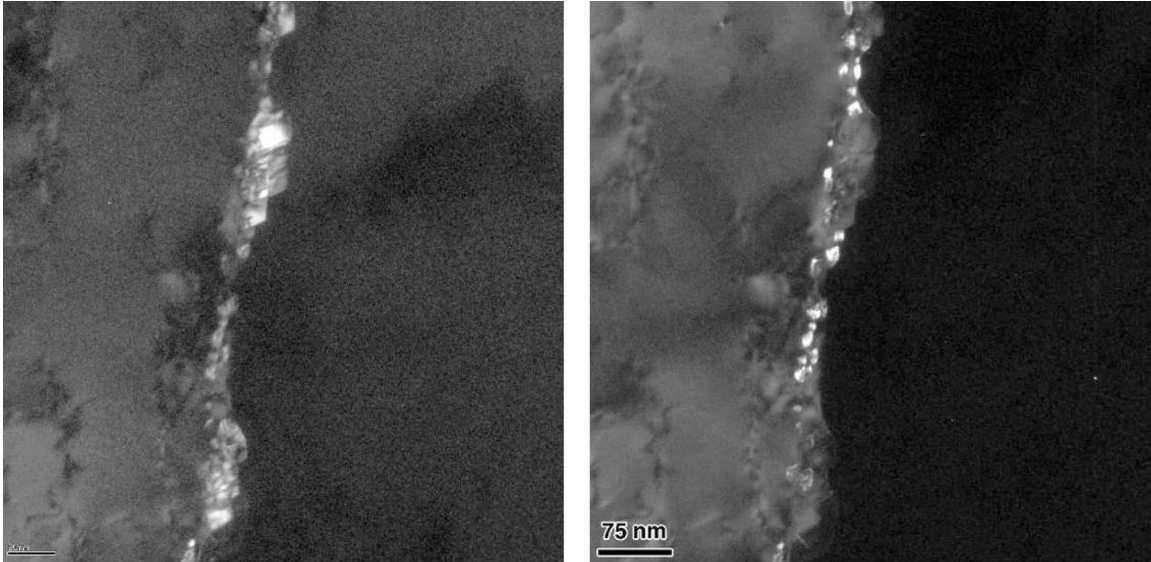


**Figure 6-4 TEM Darkfield Images Showing High Density of Fine  $M_{23}C_6$  (left) and MC Carbides (right) at Grain Boundaries.**

## **6.2 Alloy 690 CRDM Tubing Heats**

Optical metallography was performed on the six heats of alloy 690 CRDM tubing obtained from Vallourec in the longitudinal, transverse, and circumferential orientations to document grain structures, inclusions, and precipitates. Grain size and shape were reasonably consistent for all three orientations among the six heats. In addition, alloy 690 heat RE243 showed similar structures in the two different tubing thicknesses (1.0-in. and 1.4-in. thick wall) obtained. Microstructure examples for several of the heats are shown in Figures 6.5 and 6.6. Typical average grain sizes are somewhat large at approximately 100  $\mu\text{m}$  in diameter. Grain boundary carbides can be seen in the etched samples, but additional examinations by both SEM and limited TEM are required to estimate boundary coverages. Based on these examinations, three heats will be selected for solution-anneal heat treatments to remove IG carbides and maintain a similar strength level. Lower-temperature heat treatments will be performed to alter grain boundary precipitation and segregation. In the end, several of these conditions will be cold worked and machined into CT samples for future SCC crack-growth testing. Plans are for initial SCC tests to be on solution-annealed and as-received thermally treated materials followed by testing on samples made from alloy 690 material that has either been cold rolled or forged.

## **6.3 Alloy 152 Weld Metal**

Microstructural characterization was performed on the alloy 152 weld supplied by EPRI. It was made using 2.4-in.-thick plates of 304SS, alloy 152 butter passes, and welded with alloy 152. The weldment was sectioned into 0.75-in.-thick blocks (Figure 5.2) and metallographically prepared to reveal the individual weld passes and the butter zone.

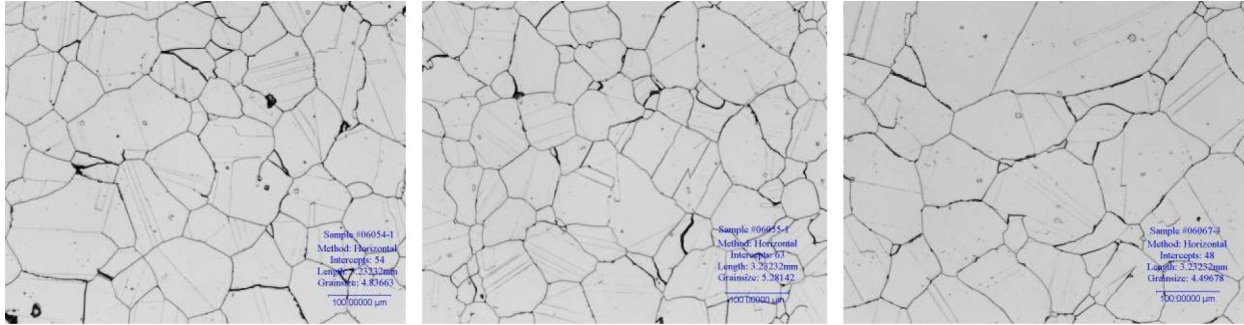


**Figure 6-5 Optical Metallographs Showing Grain Structures for Alloy 690 Heat RE243 in the Transverse (left), Longitudinal (middle), and Circumferential (right) Orientations.**

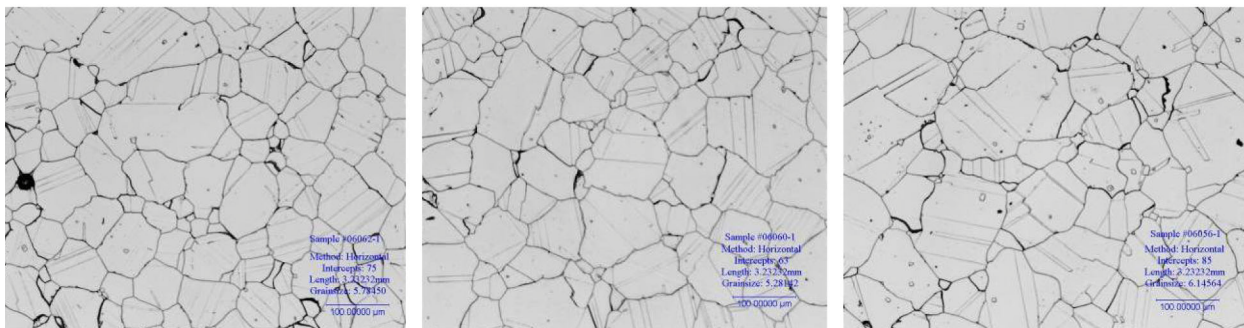


**Figure 6-6 Optical Metallographs Showing Grain Structures for Alloy 690 Heats WP016 (left), WP140 (middle), and RE169 (right).**

Optical micrographs of sections X and G were compared to study the consistency of the weld passes along the length of the weld. Though they were similar and generally one could track an individual weld pass from one end to the other, it was decided that each individual CT sample blank would need to be examined to dictate the location of the CT sample pre-crack. Locations were selected to align the pre-crack with the elongated dendrites in a single weld pass for the alloy 152 CT samples. SEM examinations were carried out in Section X and revealed a standard dendritic structure with some long dendrites interspersed with smaller ones at the junctions of the weld passes. The boundaries between dendrites were often wavy. Examples of these are seen in Figures 6.7 and 6.8. Based on SEM examination of the microstructure of the alloy 152 weld, the weld is composed of a mixture of a cellular and columnar dendritic structure with heavy precipitation in both the interiors of the dendrites and the dendritic boundaries. Backscatter electron (BSE) images of the dendrites reveal a mottled contrast that is presumed to arise due to strain in the matrix. The carbides scattered throughout the dendrites show up as dark particles in BSE images, whereas in the secondary electron (SE) images, the particles typically show up as bright particles because they are sticking out from the specimen surface. Some of the dendritic boundaries etched differently than the surrounding matrix, possibly due to either compositional changes or from precipitation on the boundaries. Additionally, EDS composition maps were made to elucidate compositional inhomogeneities in the structure and identify the major second-phase particles. As seen in Figure 6.9, there is a

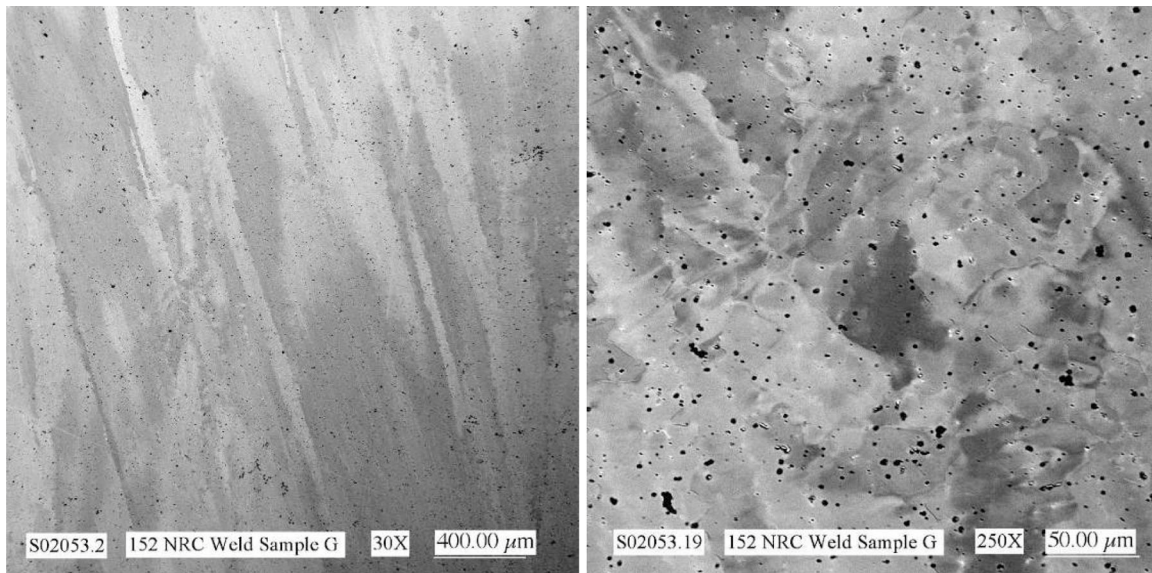


**Figure 6-7 SEM Micrographs of the Alloy 152 Weld Showing Long Dendrites (left) and Much Smaller, Equiaxed Dendrites (right). The latter are generally present at the intersection of two weld passes but some of the long dendrites pass through that region uninterrupted.**

slight amount of coring indicated in the Mn map. Coring profiles in the Fe map were complementary to the Mn map. The primary particles identified were rich in Nb (likely NbC) and Ti-Al-rich particles (likely a Ti-Al-O).

Two more thin (1/4-in.) slices were made from the weld, one being cut up for compositional analysis and the other cut for TEM sample preparation. In both cases, the cutting centered on the same weld pass as for samples C and D. Transmission electron microscopy revealed that many of the dendritic boundaries contain a widely varying distribution of metal carbides. Figure 6.10 illustrates the variability along the different boundaries in the sense that while both types of carbides exist on the boundary, they are likely to be independent of each other. In this case, a single large chromium carbide was found while numerous Nb carbides were present separate from the large Cr-carbide. As shown in Figure 6.11, both Cr- and Nb-rich carbides have precipitated along the dendritic boundaries. In some cases, though not always, Ti was found to coincide with the Nb.

Samples were also cut from the edge of the alloy 152 weld in the “transition region” from the 304SS to the buttering to the main weld. Optical examination of one of the samples that was etched revealed an altered microstructure in the 304SS. (A narrow region appears to have been melted and a dilution zone was created between the Fe-base 304SS and the butter passes to the Ni-base alloy 152 material.) No apparent difference in defects was noted compared to the main weld. A smaller sample suitable for fitting into the SEM will be examined in more detail including compositional maps. It is anticipated that crack-growth samples will also be machined to evaluate SCC susceptibility in this transition zone.

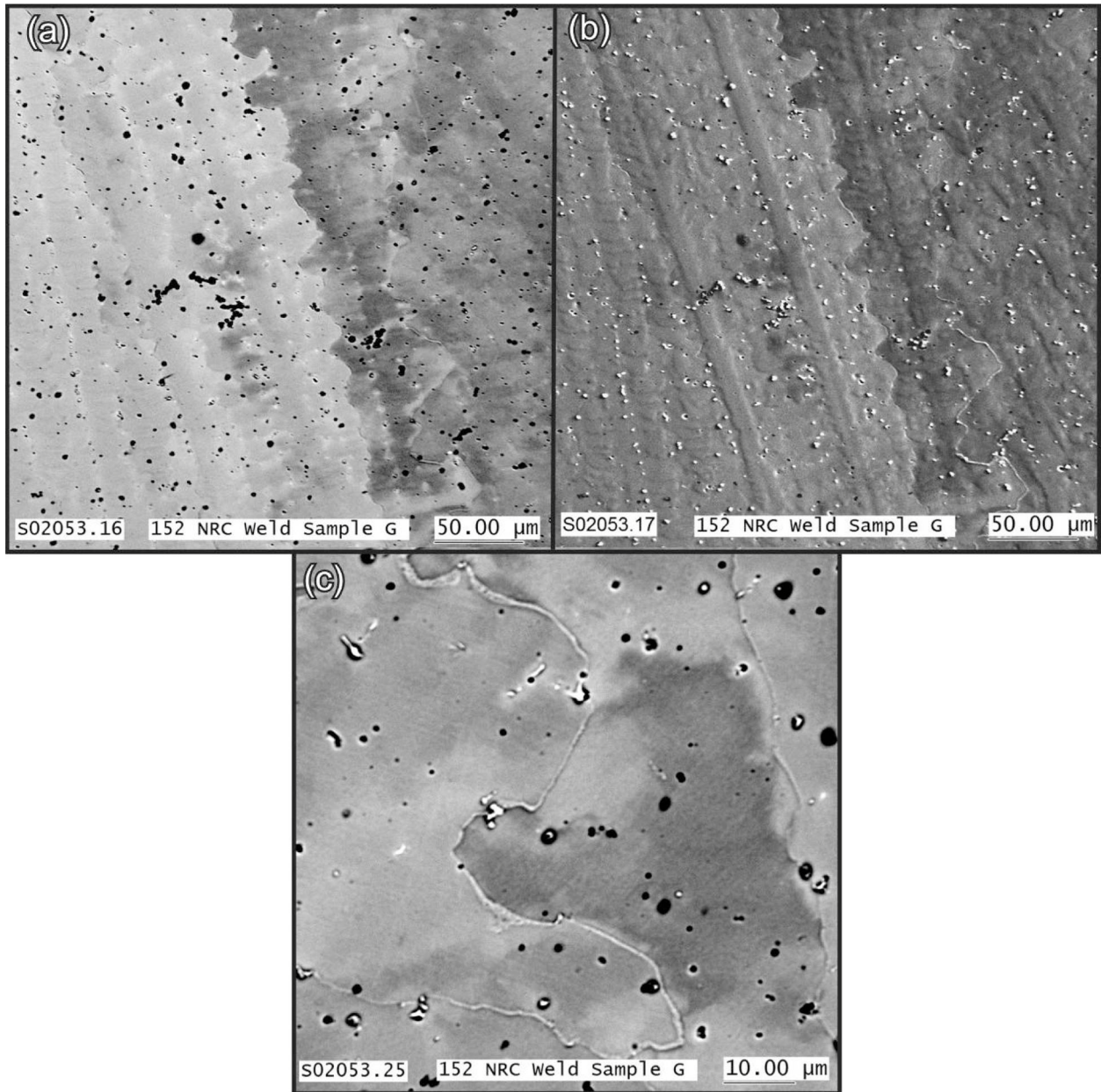


**Figure 6-8** Scanning Electron Microscope Images are shown from the Alloy 152 Weld Material. The image in (a) was taken using backscattered electrons, (b) and (c) was taken in secondary electron imaging mode.

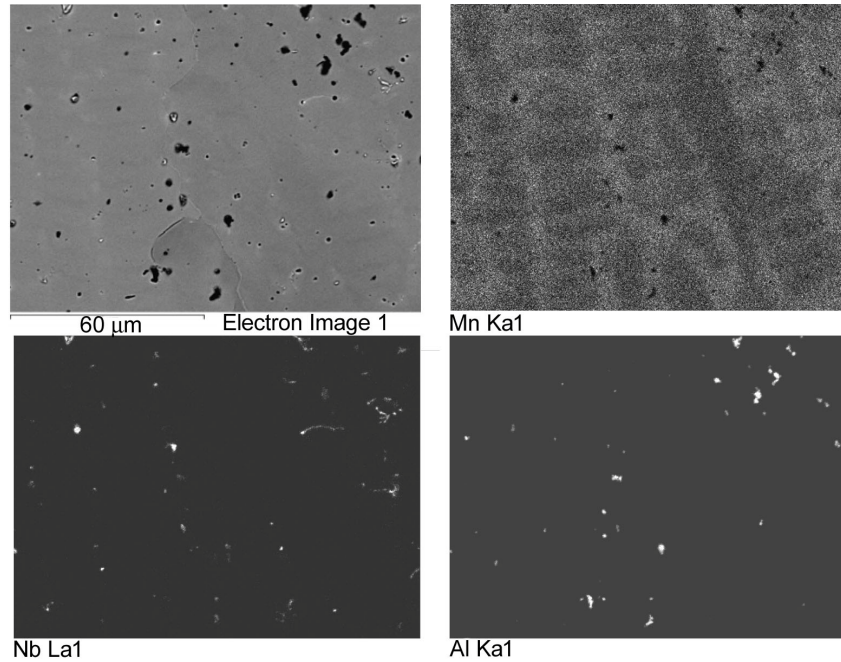


**Figure 6-9 SEM Secondary-Electron Image is shown Along with Composition Maps for Mn, Nb and Al. The Mn map indicates a slight degree of coring and the other two maps show the locations of the large NbC and the Ti-Al particles in the microstructure.**

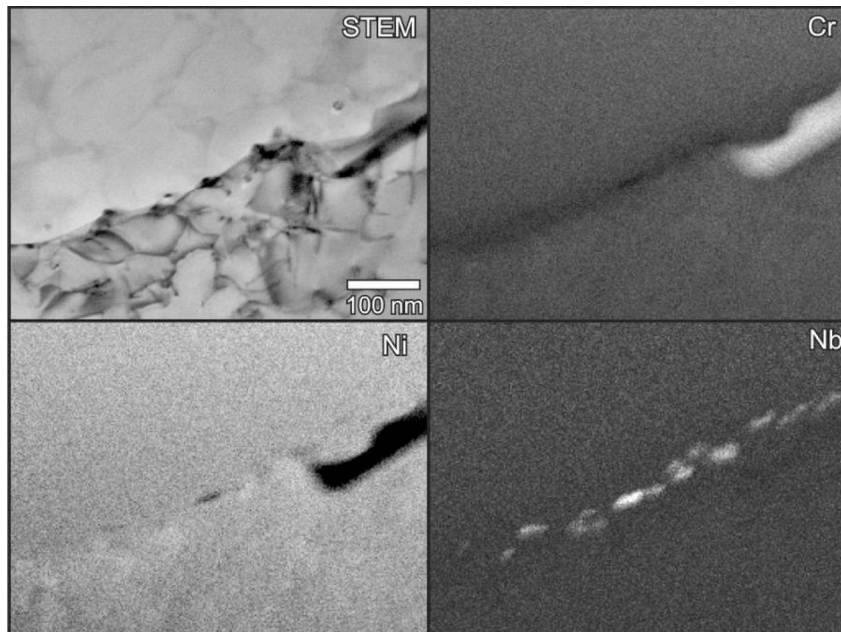


**Figure 6-10 An Example of a Different Dendritic Boundary that Shows a Single Large Cr-carbide, with Numerous Smaller Nb-carbides along the Boundary. In this case, Ti was not found associated with the Nb carbides.**

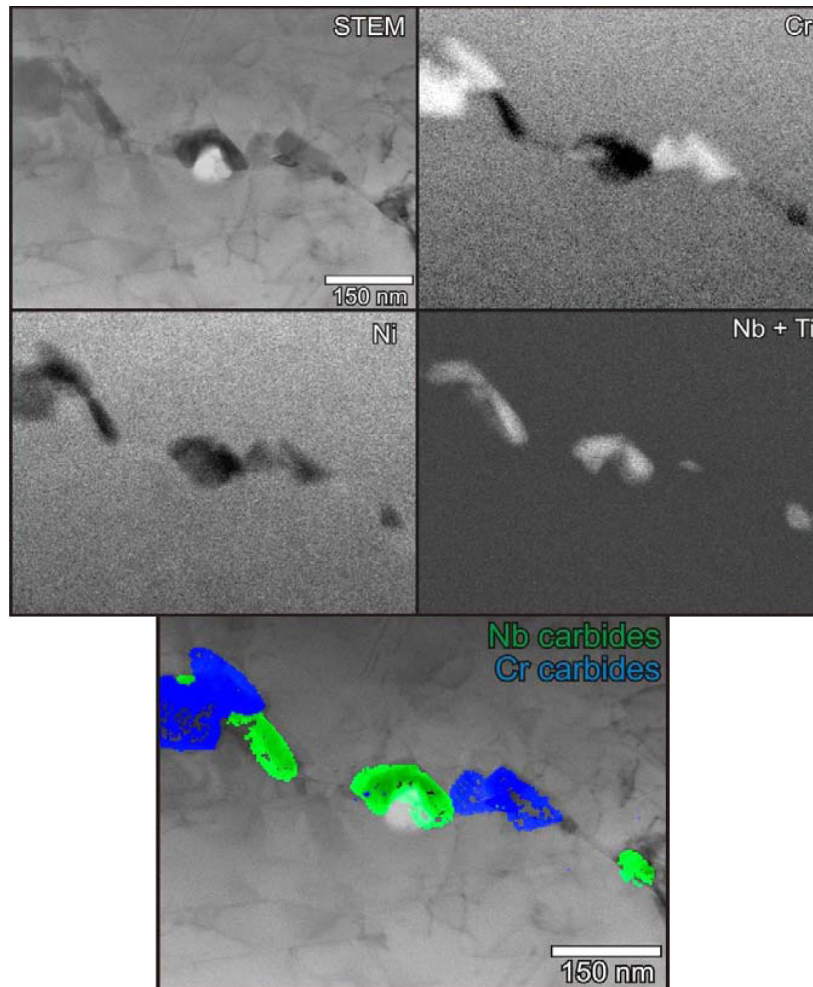


**Figure 6-11 Compositional Maps Taken in STEM Mode from the JEOL 2010F Transmission Electron Microscope Revealed that Both Cr- and Nb-rich Carbides are Present on the Boundary Between Two Dendrites. The bottom image reveals that the two carbide phases can sometimes be superimposed with each other. In this example, Nb and Ti were associated with the same particles.**

## 6.4 Crack-Tip Examinations

The fundamental basis for mechanistic understanding and modeling of stress corrosion cracking remains in question for many systems. Specific mechanisms controlling SCC can vary with changes in alloy characteristics, applied/residual stress, or environmental conditions. Local crack electrochemistry, crack-tip mechanics, and material metallurgy are the main factors controlling crack growth. The local crack conditions, especially at the tips, are difficult or impossible to measure in actively propagating cracks. Nevertheless, it is essential to quantitatively interrogate the crack-tip conditions if mechanistic understanding is to be obtained. The present approach of post-test crack characterization is an attainable step in this process.

A major recent advance has been the ability to investigate SCC cracks and crack tips using analytical transmission electron microscopy (ATEM). ATEM enables the characterization of trapped solution chemistries, corrosion product compositions and structures, composition gradients, and defect microstructures along the crack walls and at the crack tip. A wide variety of methods for imaging and analyses at resolutions down to the nanometer scale and below can be used to examine the crack and corrosion film characteristics. A critical aspect of the recent work has been the development of sample preparation methods in which the crack corrosion products are protected during the ion-thinning process by embedding the cracks with a low-viscosity thermoplastic resin. This capability combined with modern ATEM techniques has enabled new insights into corrosion processes occurring at crack tips and is being used to identify mechanisms controlling SCC in service components. A key part of this work has been direct comparisons between service components with cracks produced under complex, historically varied conditions and well-controlled laboratory test samples.

The objective of this brief section is to highlight new results focused on IGSCC cracks in austenitic stainless steels produced during laboratory crack-growth tests as part of this project. Prior work at PNNL has examined cracked components removed from BWR (i.e., stainless steel piping, core shroud, and top guide materials) and PWR (stainless steel baffle bolt, alloy 600/182 upper head penetration, and numerous alloy 600 steam generator tube materials). In addition, selected examinations have been performed on laboratory SCC CGR through collaborative interactions with GEG. Crack and crack-tip characterizations have been performed on CW304SS, CW316LSS, and sensitized 304SS after testing in BWR oxidizing water at high ECPs. A key missing aspect has been the examination of cracks produced at low ECPs either BWR-HWC or PWR primary water conditions. The SCC CGR tests CT005 and CT008 on CW316LSS under BWR-HWC conditions provided a unique opportunity for such characterizations to be accomplished.

Cross-section samples for ATEM characterization were prepared by removing small pieces containing selected crack tips from metallographically polished samples following vacuum impregnation with a low-viscosity thermosetting resin. The small slices were then glued to 3-mm-diameter Mo washers (the size of a TEM disk), with the crack tips at the disk centers. After trimming edges and flat polishing to  $\sim 100\ \mu\text{m}$  total thickness, the samples were dimple-ground from the washer sides and finished by low-angle ion micromilling with 2 to 5 KeV argon ions. Repeated cycles of ion thinning and TEM were used to progressively thin and examine multiple crack-tip areas or other crack locations of interest.

ATEM characterizations were performed using a 200-kV field-emission-gun TEM with a thin-window, energy-dispersive x-ray spectrometer (EDS) and a parallel-detection electron-energy-loss spectrometer (PEELS) for microchemical analysis. Besides conventional brightfield and precipitate darkfield imaging, characterization methods included crystal lattice imaging with Fourier-transform diffraction analysis, fine-probe (0.7-nm diameter) compositional analysis by EDS and PEELS, and parallel-beam diffraction from selected sample areas as small as  $\sim 6\ \text{nm}$  in diameter. Stereoscopic TEM photographs were used to observe finely porous structures in crack oxides. A Fresnel (off-focus) image contrast method was employed to reveal fine pores and other structures as small as 1 nm. Computer-controlled EDS mapping in a scanning transmission (STEM) mode was also extensively used to observe compositional variations along cracks and leading grain boundaries at resolutions down to  $\sim 2\ \text{nm}$ .

The crack-growth test sample CT005 was a 0.5T CT sample of CW316LSS tested under BWR-HWC conditions at 288°C (550°F) for the final ~1 mm of crack length (see Figure 4.7). The cracks were examined by OM and SEM after the sample was metallographically polished on one side. Figure 6.12(a) shows a low-magnification SEM overview of the crack from the machined pre-crack notch to the crack tip. The crack appearance suggests mixed-mode IG and TG cracking. Also, the crack seen in this section view shows apparently isolated segments separated by ductile ligaments near the tip probably caused by crack branching above or below the sectioning plane. The cracks appeared open and filled with the embedding epoxy resin used before sectioning. Cross-section TEM samples of the crack-tip region were prepared by the usual methods including dimple-grinding and ion micromilling. Figure 6.12(b) shows SEM images of the first successful sample before final ion milling. The sample is shown from the dimpled washer side, and contains a hole that developed in the metal near the crack tip during initial ion milling. The SEM images of the crack-tip region at higher magnifications indicate a highly deformed metal structure. The cracks in this region appear segmented as described above and appear mostly IG with just a few TG examples. TEM examinations focused on the tip region. Iterated cycles of examination and retouch thinning were used to examine the microstructures of crack walls that were protected by the embedding resin as well as the two tip areas (tips 1 and 2).

Cracks observed near the furthest advanced tip were initially filled with the epoxy embedding resin used in sample preparation. In some areas, the epoxy protected the narrow corrosion films along the crack walls until the structures were thin enough for TEM observations. Uniform 8- to 10-nm wide oxide films were found on the metal crack walls, and 20- to 40-nm diameter oxide crystallites on the outer surfaces of the oxide films. The wall-oxide films appeared nonporous and had abrupt, planar interfaces with unaltered metal. EDS analyses including high-resolution STEM/EDS maps and line profiles taken across the oxide showed Cr/Fe ratios up to ~1 in the wall-oxide films. This indicates a considerable Cr enrichment in the oxide films compared to the metal matrix (Cr/Fe ~0.2). Ni also appeared slightly enriched in a narrow layer at the metal/oxide interfaces. Apart from the local Ni enrichment at the metal/oxide interfaces, the alloy compositions beyond a few nm into the metal showed no detectable change. No environmental impurities were detected in either oxide. EDS analyses also showed that the oxide crystallites on the film surfaces were Fe rich, with metal atom ratios similar to that of the alloy.

Electron diffraction analyses of the oxide crystal structures, performed by nano-area diffraction and darkfield imaging methods, identified the wall films as oriented single-crystal rocksalt-type oxide (FeO/NiO type), and the Fe-rich crystallites as spinel. This is illustrated in Figure 6.13 by differences between darkfield images taken with spinel-only and FeO + spinel type reflections. [Note: The cubic spinel and FeO-type crystal structures produced by corrosion of Fe-Ni-Cr alloys have the same lattice frameworks with different atomic site occupancies of the ordered cations. The FeO-type spots in diffraction patterns are a subset of the spinel reflections, so that oxide darkfield images can be taken to show the spinel regions only or both structures together.] Both oxide structures in the open cracks had cube-on-cube orientation relationships with the adjacent metal grains.

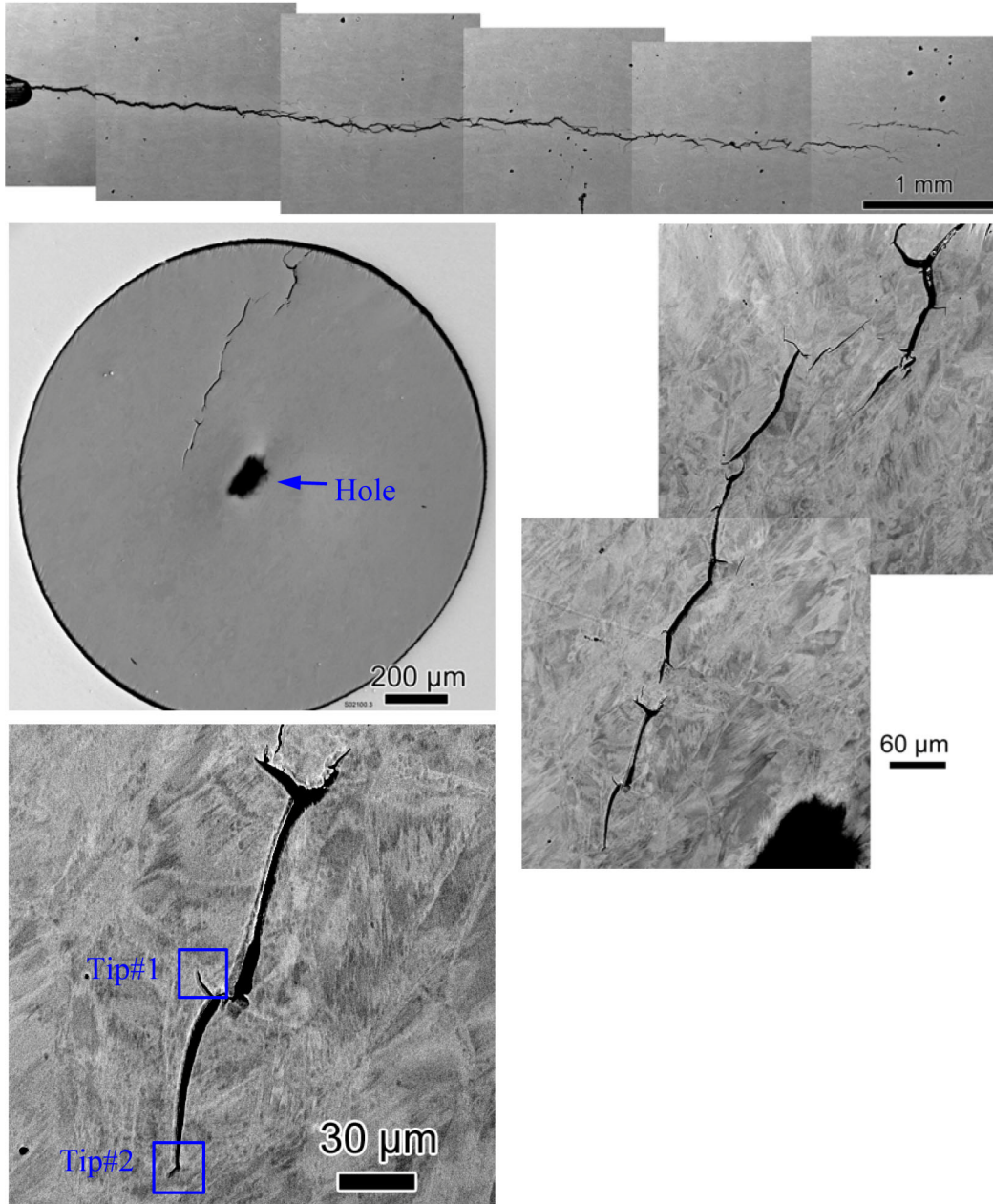


**Figure 6-12 Overall Composite Image of Crack in Cross-Section for Crack-Growth Sample CT005 is Shown in (a) with SEM of TEM sample 6025B, region near crack tip in (b). Perforation in TEM disc near the center was produced during ion milling. Higher magnification BSE images of crack-tip region are documented in (c) and (d). Metal matrix appears to be highly strained causing the contrast in the BSE images.**

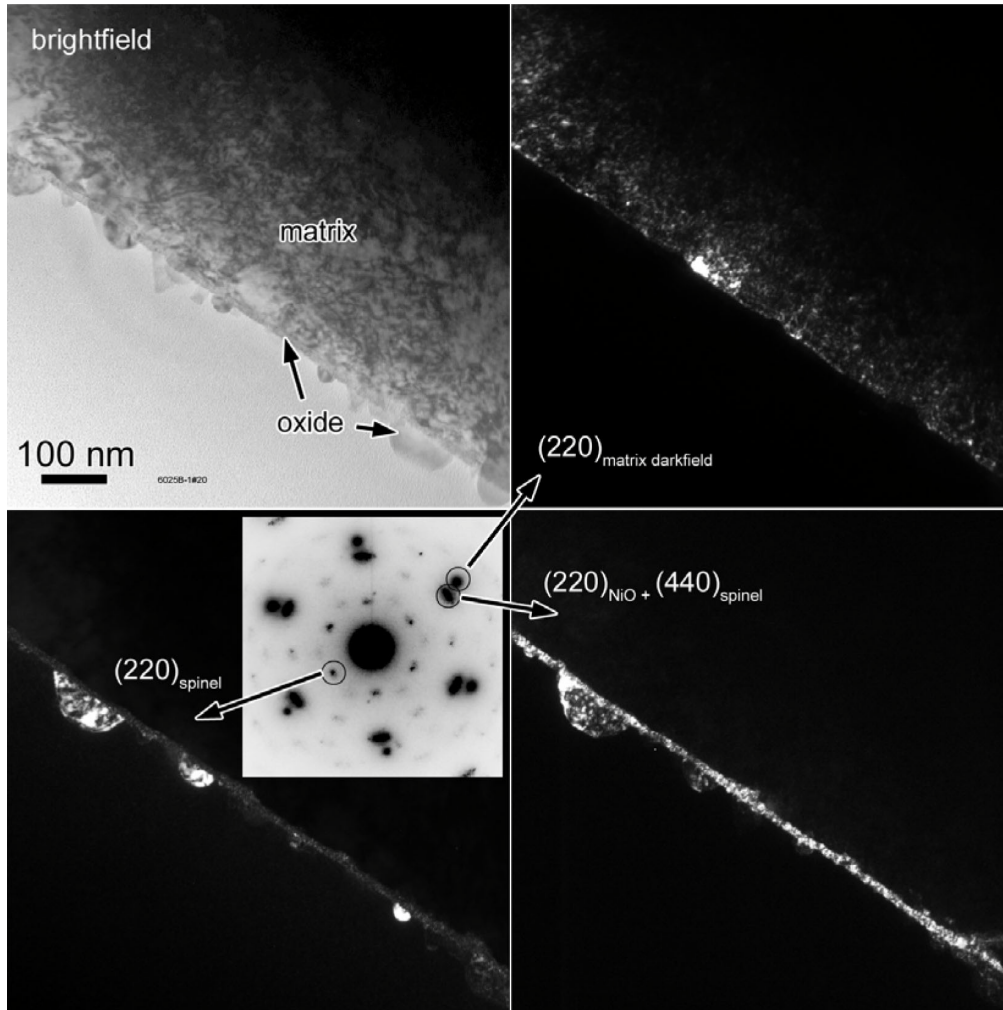


**Figure 6-13 Crack Wall Oxides in Cold-Worked 316LSS Test Sample CT005. (a) TEM brightfield image showing strained matrix and surface oxide. (b) Darkfield image taken with matrix reflection. (c) Darkfield image taken with spinel-only reflection, highlighting crystallites on outer oxide surface. (d) Darkfield image taken with coincident spots from spinel and FeO-structure oxide. Differences between (c) and (d) identify uniform oxide layer as FeO-type rather than spinel. Inset diffraction pattern from [111] matrix and parallel-oriented oxides.**

Tip#1 in this sample ended just past a grain-boundary triple-point as shown in Figure 6.14, with very short branches on both grain boundaries after the intersection. The boundary inclinations differed slightly so that different tilts were needed to bring the boundaries on edge. The image in Figure 6.14(a) shows the body of the crack on edge. A narrow gap along the crack center continues between the wall oxide layers until the crack intersects the grain boundary junction. The curved appearance of the grain boundary near the junction point is due to the oxide formed near the crack tip. When tilted to an inclined position as in Figure 6.14(c), the crack has a porous appearance caused by the Fresnel contrast at slight underfocus.

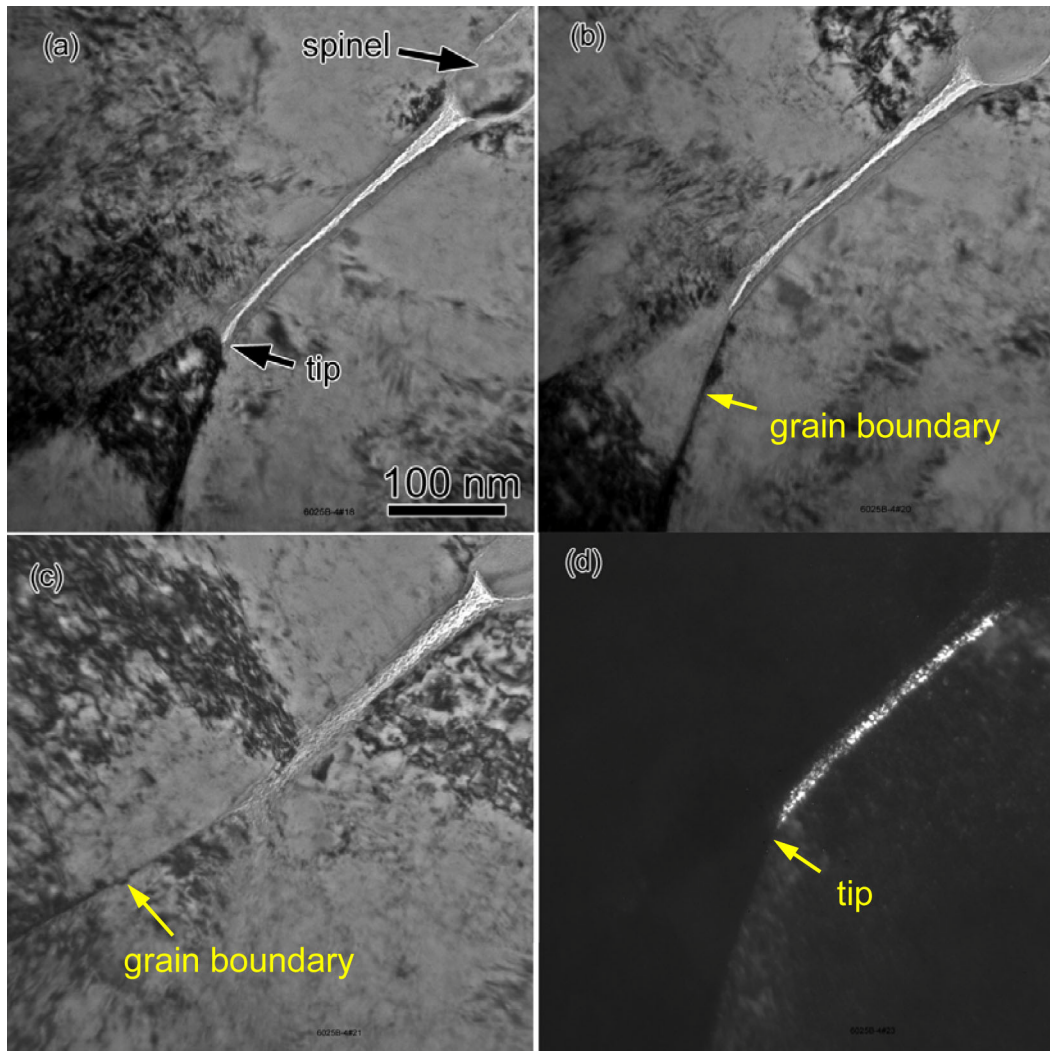


**Figure 6-14 Crack Tip#1 in Cold-Worked 316LSS Test Sample CT005. (a-c) TEM brightfield images taken at different tilts to show tip splitting at grain-boundary triple-point junction. Slightly underfocused image shows gap extending along crack center almost to tip. (d) FeO darkfield image highlighting oriented oxide layer on one side of crack. Oxide ends at tip.**

Darkfield images of the oxide films at the tip (example in Figure 6.14d) showed that the oriented FeO-type oxide continued to the leading edges of the cracks. EDS maps of this tip show the strong Fe depletion of the wall oxide at the tip, no depletion of Cr, and local enhancement of Ni along the metal/oxide interface.

Tip #2 in Figure 6.15 ended with a sharp point along a particle-free section of grain boundary. This crack also appeared bulged around oversized spinel particles near the tip. It contained an epoxy-filled gap nearly to the end, and oriented narrow uniform films of Cr-rich oxide up to the tip. An oxide darkfield image in Figure 6.15(b) shows the uniform (single-crystal) oxide layer on one side of the crack. EDS maps revealed these oxide layers were present all the way to the

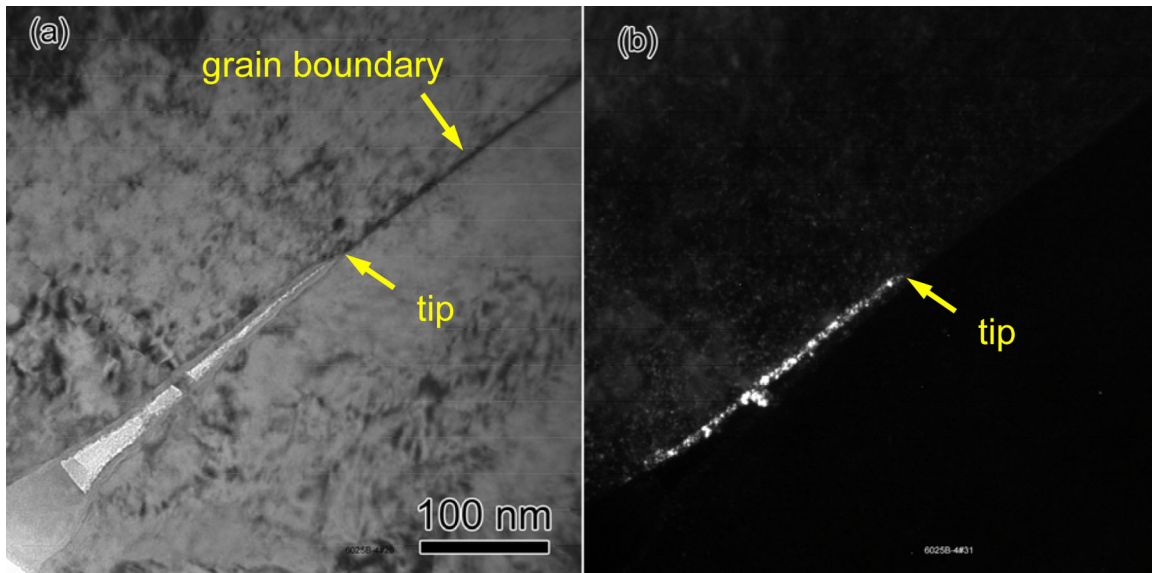


**Figure 6-15 Crack Tip #2 in Cold-Worked 316LSS Test Sample CT005. (a) TEM brightfield image with grain boundary viewed on edge. (b) FeO darkfield image highlighting oriented oxide layer on one side of crack.**

crack tip. They also show strong Fe and Ni depletion of the oxide at the tip, and enhanced Ni at the metal/oxide interfaces at the sides and just ahead of the tip. Mo segregation is seen along the leading grain boundary. ED scans were taken across the oxide near the tip, across the leading grain boundary, and along the crack centerline and the leading grain boundary. The profiles show Cr-rich oxide at the center of the crack, Ni enhanced at the edges and along the leading grain boundary, and Ni enhancement just ahead of the oxide for a distance of ~20 nm.

As noted early in this section, crack-tip examinations have been a major continuing activity at PNNL for nearly a decade. The current characterizations on CW316LSS cracked under BWR-HWC conditions is an important next step in these studies and were supported through Rolls Royce Limited as part of a program on mechanisms of stress corrosion cracking. It will enable important comparisons to extensive work on 304SS and 316SS samples cracked in BWR oxidizing water environments. Mechanisms of SCC for stainless steels in low-ECP BWR or PWR conditions may become increasingly important as plant issues are identified. ATEM has the ability to reveal new details of SCC structures that cannot be detected by other methods. The current observations must be considered work in progress and additional work is needed to properly establish mechanisms controlling IGSCC. In particular, ATEM characterizations must continue to be performed on samples where mechanisms are better distinguished and controlling variables are systematically varied such as our ongoing crack-growth-rate experiments. In addition to selected experiments on austenitic stainless steels, plans are to investigate SCC crack-tip structures in alloy 690 and 152 samples and compare to previous results on alloy 600 and 182 materials. Isolated examinations may also be performed on cracked CRDM welds removed from PWR service.

## 7 Conclusions

Three CGR test systems have been assembled with capabilities qualified through experiments first on CW stainless steels in high-purity BWR environments followed by tests on CW alloy 600 and alloy 182 weld metal as part of round-robin collaborations. The CGR tests on stainless steels evaluated stress intensity, cyclic loading, electrochemical potential (ECP), and sulfate additions on SCC propagation rates. Reproducible dcpd crack-length measurements were demonstrated with resolution down to micrometer dimensions. Unexpected high crack-growth rates at low ECPs in BWR hydrogen water chemistry (HWC) conditions were observed for one CW 316LSS heat. Two independent experiments were performed on this material over a range of stress intensities and hydrogen levels showing propagation rates near  $10^{-7}$  mm/s under low ECP conditions. This is a small decrease (2–3X) in CGR from the BWR oxidizing conditions (2000 ppb O<sub>2</sub>). The other two CW 316SS heats evaluated exhibited the expected significant reduction in CGR (50–100X) when oxygen is removed and hydrogen added to the high-purity BWR water. Round-robin CGR testing (led by the International Cooperative Group on Environment-Assisted Cracking) was performed on alloy 600 and alloy 182 materials. Experiments were conducted in BWR oxidizing water for both alloys and in simulated PWR primary water for the alloy 182 weld metal. Results from the round robin tests demonstrated state-of-the-art capabilities for the PNNL systems and testing methodology through comparisons with other participating laboratories in the United States, Europe, and Japan. After round robin testing, the influence of H<sub>2</sub> level in PWR primary water on SCC was examined using the alloy 182 material documenting higher propagation rates at lower H<sub>2</sub> values that correspond to ECPs near the Ni/NiO stability line. Finally, initial tests on alloy 152 weld metal and alloy 690 CRDM materials are underway and preliminary data were described. A wide range of characterization activities has been completed on project materials including detailed microstructural studies of alloy 182 and 152 weld metals. High-resolution, SCC crack-tip measurements have also been performed for the first time on a CW316LSS after CGR testing in a BWR-HWC environment.



**BIBLIOGRAPHIC DATA SHEET**

(See instructions on the reverse)

NUREG/CR-7103

2. TITLE AND SUBTITLE

Pacific Northwest National Laboratory Investigation of Stress Corrosion Cracking in Nickel-Base Alloys, Volume 1

3. DATE REPORT PUBLISHED

MONTH

YEAR

September

2011

4. FIN OR GRANT NUMBER

5. AUTHOR(S)

S.M. Bruemmer and M. B. Toloczko

6. TYPE OF REPORT

NUREG/CR

7. PERIOD COVERED (Inclusive Dates)

10/1/2004 to 9/30/2006

8. PERFORMING ORGANIZATION - NAME AND ADDRESS (If NRC, provide Division, Office or Region, U.S. Nuclear Regulatory Commission, and mailing address; if contractor, provide name and mailing address.)

Pacific Northwest National Laboratory  
PO BOX 999  
Richland, WA 99352

9. SPONSORING ORGANIZATION - NAME AND ADDRESS (If NRC, type "Same as above"; if contractor, provide NRC Division, Office or Region, U.S. Nuclear Regulatory Commission, and mailing address.)

Division of Engineering  
Office of Nuclear Regulatory Research  
U.S. Nuclear Regulatory Commission  
Washington D.C. 20555-0001

10. SUPPLEMENTARY NOTES

11. ABSTRACT (200 words or less)

This report documents work conducted by Pacific Northwest National Laboratory (PNNL) during calendar years 2005 and 2006 under contract to the NRC. Testing conducted during this period consisted of assembling crack growth rate testing systems, verification of system capability and measurement resolution, crack growth rate testing, and material characterization. Initial tests included cold worked alloy 600 and alloy 182 weld metal. Tests were also conducted on the higher chromium containing alloy 690 control rod drive mechanism (CRDM) tubing and alloy 152 welds from industry mockups of replacement components. Although results of these tests along with compositional maps and initial high resolution imaging of crack tips suggest that the higher chromium base and weld metals are more resistant to PWSCC, additional testing and analyses will be conducted on alloy 690 as well as alloy 152 and 52 weld samples to determine the factors that affect PWSCC resistance in the high chromium weld alloys. The combination of microstructural and crack tip analyses on test materials with known crack growth rates will contribute to both industry-led research and support inspection criteria for existing and new reactors.

12. KEY WORDS/DESCRIPTORS (List words or phrases that will assist researchers in locating the report.)

Pacific Northwest National Laboratory  
Primary Water Stress Corrosion Cracking  
PWSCC  
Crack growth rate testing  
Alloy 600  
Alloy 182  
Alloy 82  
Alloy 690  
Alloy 52  
Alloy 152

13. AVAILABILITY STATEMENT

unlimited

14. SECURITY CLASSIFICATION

(This Page)

unclassified

(This Report)

unclassified

15. NUMBER OF PAGES

16. PRICE



Federal Recycling Program





**UNITED STATES  
NUCLEAR REGULATORY COMMISSION**  
WASHINGTON, DC 20555-0001  
-----  
OFFICIAL BUSINESS

**NUREG/CR-7103, Vol. 1**

**Pacific Northwest National Laboratory Investigation of  
Stress Corrosion Cracking in Nickel-Base Alloys**

**September 2011**